

# Segmentation and Visualization for Cardiac Ablation Procedures

by

Michal Depa

B.S., McGill University (2008)

Submitted to the Department of Electrical Engineering and Computer Science

in partial fulfillment of the requirements for the degree of

Master of Science in Electrical Engineering and Computer Science

at the

MASSACHUSETTS INSTITUTE OF TECHNOLOGY

February 2011

© Massachusetts Institute of Technology 2011. All rights reserved.

Author .....  
Department of Electrical Engineering and Computer Science  
January 28, 2011

Certified by .....  
Polina Golland  
Associate Professor  
Thesis Supervisor

Accepted by .....  
Terry P. Orlando  
Chairman, Department Committee on Graduate Theses



# Segmentation and Visualization for Cardiac Ablation Procedures

by

Michal Depa

Submitted to the Department of Electrical Engineering and Computer Science  
on January 28, 2011, in partial fulfillment of the  
requirements for the degree of  
Master of Science in Electrical Engineering and Computer Science

## Abstract

In this thesis, we present novel medical image analysis methods to improve planning and outcome evaluation of cardiac ablation procedures. Cardiac ablation is a common medical procedure that consists of burning cardiac tissue causing atrial fibrillation, or irregular contractions of the heart's atria.

We first propose a method for the automatic delineation of the left atrium in magnetic resonance (MR) images acquired during the procedure. The high anatomical variability of the left atrium shape and of the pulmonary veins that drain into it presents significant difficulties for cardiac ablation. Consequently, accurate visualization of the patient's left atrium promises to substantially improve intervention planning. We perform the segmentation using an automatic atlas-based method, which makes use of a set of example MR images in which the left atrium was manually delineated by an expert. We demonstrate that our approach provides accurate segmentations that are also robust to the high anatomical variability of the left atrium, while outperforming other comparable methods.

We then present an approach to use this knowledge of the shape of the left atrium to aid in the subsequent automatic visualization of the ablation scars that result from the procedure and are visible in MR images acquired after the surgery. We first transfer the left atrium segmentation by aligning the pre and post-procedure scans of the same patient. We then project image intensities onto this automatically generated left atrium surface. We demonstrate that these projections correlate well with expert manual delineations. The goal of the visualization is to allow for inspection of the scar and improve prediction of the outcome of a procedure. This work has a potential to reduce the considerable recurrence rates that plague today's cardiac ablation procedures.

Thesis Supervisor: Polina Golland  
Title: Associate Professor



## Acknowledgments

I would like to start by thanking my parents Teresa and Jurek. Your years of love and unwavering support shaped me into the person I am today. I cannot express in words my gratitude for the sacrifices you made for me. Without them I would never have been able to make it even nearly this far. I would also like to thank my dear sister Małgosia who has always been there for me. Kocham Was.

None of this work would have been possible without the unconditional support of my advisor, Prof. Polina Golland. I would like to thank you for, at times despite my best efforts, keeping me focused and on track. Your enthusiasm and ideas have been indispensable to me. Thank you for always challenging me and helping make the last two years the most interesting and stimulating time of my life.

This work would also not have been possible without my officemates' extremely high tolerance to interruptions. Thank you for being willing to help me whenever I needed it. I would also like to thank all of the current and past members of the Medical Vision Group, the MIT Computer Vision community in general and all of my collaborators for their input and fresh ideas.

Last but definitely not the least, I would like to thank all of my great friends who made this journey rank highly amongst the best times of my life. Without naming names, this is to all the awesome and fun-loving G9ers, slightly crazy G7ers, at times dysfunctional Burton1 alumni, classy TPPers, life-long friends back in Montréal and everyone in between. You know who you are. Thanks for all the good times!



# Contents

<b>1</b>	<b>Introduction</b>	<b>13</b>
<b>2</b>	<b>Prior Work</b>	<b>17</b>
2.1	Left Atrium Segmentation . . . . .	17
2.2	Cardiac Scar Visualization . . . . .	18
<b>3</b>	<b>Registration</b>	<b>21</b>
3.1	Background . . . . .	21
3.1.1	Rigid and Affine Registration . . . . .	21
3.1.2	Non-Rigid Registration . . . . .	23
3.1.3	Demons Registration Algorithm . . . . .	25
3.1.4	Groupwise Registration . . . . .	27
3.2	Intersubject Registration . . . . .	28
3.2.1	Methodology . . . . .	28
3.2.2	Implementation . . . . .	31
3.2.3	Results . . . . .	31
3.3	Intermodality Registration . . . . .	34
3.3.1	Methodology and Implementation . . . . .	35
3.3.2	Results . . . . .	35
3.4	Summary . . . . .	36
<b>4</b>	<b>Atlas-based Segmentation</b>	<b>39</b>
4.1	Background . . . . .	39

4.1.1	Segmentation with Parametric Atlases . . . . .	39
4.1.2	Segmentation with Nonparametric Atlases . . . . .	41
4.2	Robust Left Atrium Segmentation . . . . .	44
4.2.1	Methodology . . . . .	44
4.2.2	Results . . . . .	45
4.3	Summary . . . . .	52
<b>5</b>	<b>Ablation Scar Visualization</b>	<b>53</b>
5.1	Methodology . . . . .	53
5.2	Results . . . . .	56
5.3	Summary . . . . .	58
<b>6</b>	<b>Discussion and Conclusions</b>	<b>61</b>
6.1	Robust Left Atrium Segmentation . . . . .	61
6.2	Ablation Scar Visualization . . . . .	63

# List of Figures

1-1	Manual segmentations of the left atrium in three different subjects. . .	14
1-2	Showcase of results obtained using the methods presented in this thesis.	16
3-1	Registration results for three different subject pairs. Shown are (a) fixed and (b) moving MRA images, as well as checkerboard mosaics showing registration results after (c) affine and (d) non-rigid diffeomorphic demons registration. Sagittal cross sections are shown for subjects 1 and 2. Axial cross sections are shown for subject 3. . . . .	33
3-2	Dice overlap scores of the left atrium in 15 pairs of MRA images before alignment (red), after affine registration (green) and after non-rigid registration (blue). . . . .	34
3-3	Checkerboard mosaics (a) before and (b) after affine registration of MRA and DE-MRI image pairs of three different subjects. Blue arrows show areas on the surface of the left atrium where the alignment considerably improved after affine registration, while green arrows indicate locations where there was little or no improvement. . . . .	37
4-1	Construction and use of a traditional parametric atlas for segmentation.	40
4-2	Construction and use of a nonparametric atlas for segmentation. . . .	42
4-3	Example segmentations of four different subjects: (a) expert manual segmentation (MS), (b) weighted voting label fusion (WV), (c) majority voting label fusion (MV), (d) parametric atlas thresholding (AT) and (e) EM-segmentation using the parametric atlas as a spatial prior (EM). . . . .	47

4-4	Qualitative evaluation of left atrium segmentations in three different subjects. First row shows expert manual segmentations. The corresponding automatic segmentations produced by our method are in the second row. . . . .	49
4-5	Dice scores of results for weighted voting label fusion (WV), majority voting label fusion (MV), parametric atlas thresholding (AT) and atlas-based EM-segmentation (EM). For each box plot, the central red line indicates the median, the boxes extend to the 25 <sup>th</sup> and 75 <sup>th</sup> percentiles, and the whiskers extend to the most extreme values not considered outliers, which are plotted as red crosses. Stars indicate that the weighted label fusion method achieves significantly more accurate segmentation than the baseline method (single-sided paired t-test, *: $p < 0.05$ , **: $p < 0.01$ ). . . . .	51
5-1	Percentages of manually segmented ablation scar voxels that lie within a particular distance of the automatically generated left atrium segmentations in DE-MRI images. Each box plot summarizes the results from 25 subjects; the central red line in each box represents the median, the boxes extend to the 25 <sup>th</sup> and 75 <sup>th</sup> percentiles, and the whiskers extend to the most extreme values not considered outliers, which are plotted as red crosses. . . . .	55
5-2	Comparison of projections of DE-MRI data and manual scar segmentation onto left atrium surface. Circled area indicates acquisition artifact that causes non-scar tissue to be appear enhanced in the DE-MRI image.	57
5-3	Dice overlap scores of the thresholded maximum intensity projections on the surface and the projected manual ablation scar segmentations. Shown in blue are the Dice scores produced when using the automatically determined threshold, while the overlap scores resulting from the optimal thresholds are shown in red. . . . .	59

# List of Tables

4.1	Computation times for different left atrium segmentation methods . .	52
-----	--	----



# Chapter 1

## Introduction

Heart disease is the leading cause of death in many developed countries, including the United States. Atrial fibrillation is one of the most common heart conditions. It manifests itself as irregular contractions of the heart's atria and can have serious consequences such as stroke and heart failure [4, 12]. Catheter-based radio-frequency ablation has recently emerged as a treatment for this condition. It involves burning the cardiac tissue that is responsible for the re-entry electrical currents that cause fibrillation. Even though this technique has been shown to work fairly well on atrial fibrillation patients, repeat procedures are often needed to fully correct the condition.

This thesis aims to develop techniques to enhance cardiac ablation procedures by analyzing magnetic resonance images of the patients acquired before and after the surgery. We present methods for automatic segmentation of the left atrium of the heart and the visualization of ablation scars.

There are several important challenges in the current ablation practice. One of these is the high anatomical variability in the left atrium. Specifically, the shape of the left atrium cavity, as well as the number and locations of the pulmonary veins draining into it, vary substantially across subjects. Fig. 1-1 illustrates this variability in left atria of different patients.

The high anatomical variability of the left atrium presents significant difficulties for cardiac ablation since it is commonly performed at the junction of the atrial body and pulmonary veins. Consequently, accurate visualization of the patient's left atrium

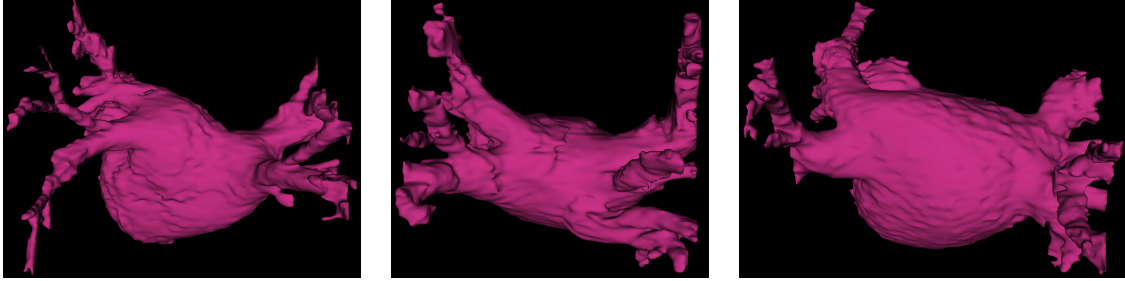


Figure 1-1: Manual segmentations of the left atrium in three different subjects.

promises to substantially improve intervention planning.

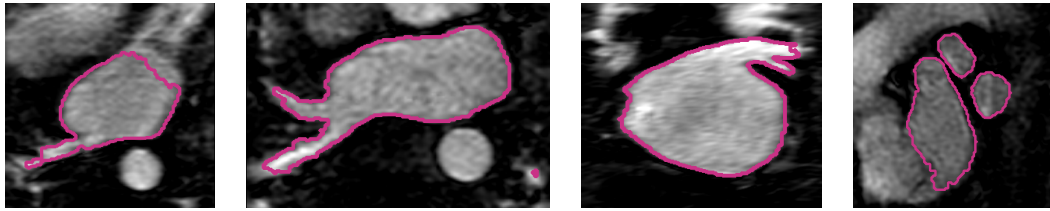
Lack of quantitative evaluation of procedures is another important challenge in the current cardiac ablation practice. Currently, there is no real way for the surgeon to evaluate the outcome of the procedure except for waiting to see if the symptoms reoccur in the patient. It is possible to visualize the ablation scar by first acquiring a contrast enhanced magnetic resonance scan of the patient’s heart using delayed enhancement magnetic resonance imaging (DE-MRI) and then segmenting the scar manually. However, this approach is not practical in a clinical setting because performing manual segmentation is a time consuming task, even for experts. It is also challenging to automatically segment the ablation scar in the DE-MRI images because of their poor resolution and contrast.

Our approach is to first segment the left atrium of the subject’s heart in a different type of routinely acquired image called magnetic resonance angiography (MRA), also referred to as a blood pool image, in which a contrast agent makes the blood pool appear at a higher intensity than the surrounding tissues. We perform the segmentation using a variant of a label fusion technique [15, 29]. The method uses a training set of MRA images from different patients with their left atria manually segmented to provide a prior for the segmentation of a new scan. We align the training images to the novel image to be segmented and apply the resulting deformations to the corresponding manual segmentation label maps to yield a set of segmentations of the left atrium in the coordinate space of the test subject. We then use a weighted voting algorithm to assign every voxel to the left atrium or background label. Our method robustly produces more accurate results than other atlas-based approaches

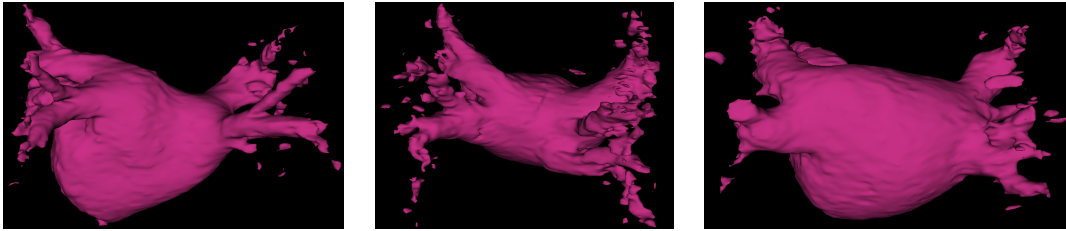
while remaining fully automatic [7].

We subsequently use the knowledge of the shape of the left atrium to aid in the visualization of the ablation scars. Effectively, the left atrium segmentation provides a spatial prior for the location of the scar, since the scar can only appear on the left atrium myocardium. We first transfer the left atrium segmentation obtained in the MRA image to the DE-MRI image of the same patient where the ablation scar is visible via registration of the two images. The knowledge of the location of the structure of interest, in our case the left atrium of the heart, restricts the search for the scar to locations where it is expected to appear. This approach prevents false positives in the neighboring structures and spurious detections due to high noise. Fig. 1-2 illustrates examples of the left atrium segmentations and ablation scar visualizations we obtain using the methods described in this thesis.

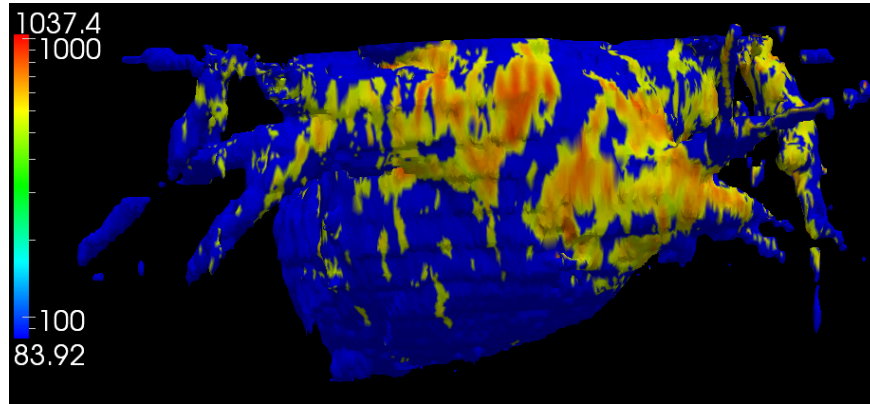
This thesis is organized as follows. We begin by discussing prior work in atrial segmentation and ablation scar visualization in Chapter 2. Chapter 3 begins by a broad review of registration algorithms before describing the specific approaches we adopt for registration of images in this thesis. In Chapter 4, we discuss segmentation algorithms and present our method for automatically delineating the left atrium in MRA images. It is followed by a description of our ablation scar visualization techniques in Chapter 5. Finally, we conclude with a summary of this work and a discussion of future research directions in Chapter 6.



(a) Automatic left atrium segmentation outlines



(b) Renderings of automatic left atrium segmentations



(c) Ablation scar visualization

Figure 1-2: Showcase of results obtained using the methods presented in this thesis.

# Chapter 2

## Prior Work

In this chapter, we review relevant work in segmentation of the left atrium and cardiac scar visualization.

### 2.1 Left Atrium Segmentation

To the best of our knowledge, automatic visualization techniques for ablation scars have not been demonstrated before, but there have been several efforts to automatically segment the left atrium. One approach is whole heart segmentation, where all of the heart chambers, and sometimes other structures, are included in a single model and segmented simultaneously. Unfortunately, most whole heart segmentation methods do not model the pulmonary veins of the left atrium [11, 36]. An exception is [24], where the geometrical model of the heart constructed from CT images includes the pulmonary veins. However, the approach involves building a mean shape model that will face considerable challenges in the presence of topological differences in anatomy.

There has also been interest in segmenting the left atrium in MRA images. One approach is to first segment the whole blood pool by intensity thresholding and then to separate it into the different heart chambers by making cuts at narrowings [20]. More specifically, the diameter of the blood pool at every point was obtained by computing the Euclidean distance map of the initial blood pool segmentation. This diameter was then used to find the locations of the narrowings. Finally, neighboring

components were merged if the narrowing separating them was larger than a certain threshold. The method also allowed for user interaction to correct any errors made by the algorithm. This approach suffers from the need to set several arbitrary thresholds manually. Additionally, there is no narrowing of the blood pool at the boundary between the left atrium and ventricle, so it would not be possible for the algorithm to yield a segmentation of the true atrial body.

This method was improved on in [21] by several modifications, including using a larger neighborhood to compute the distance transform maxima and a different method for assigning voxels to subdivisions. A level set method for segmenting the atrial body without the pulmonary veins was also presented. In this approach, a surface evolves from a user-selected seed point first using a speed function based on the Euclidean distance transform and then one based on the local intensity gradient with a strong constraint on its curvature, which prevents it from leaking into the pulmonary veins. In this work as well, several threshold values need to be set by the user. In contrast, the solution we present in Chapter 4 is fully automatic and its parameters only need to be calibrated for each acquisition protocol.

## 2.2 Cardiac Scar Visualization

There has been a lot of interest in visualizing ablation scars in the clinical community. An important advancement was the development of methods for the electroanatomic mapping of cardiac chambers in the MR environment [10, 30]. These maps are produced by touching with a mapping catheter many locations of the myocardium of a cardiac chamber while recording the electric potential at each such point. The output is a map of potentials of the entire surface of interest. It has been demonstrated that electroanatomic maps help to accurately identify scar tissue on the left ventricle myocardium in animal models such as swine [10]. The approach involves mounting microcoils on the mapping catheter, then tracking it in real-time by continuously acquiring and processing MR data. In subsequent work, the idea was expanded to tracking both the mapping and RF ablation catheters simultaneously using the same

method [30]. Although electroanatomic mapping was shown to provide accurate information on the location and extent of the scar, its invasive nature presents an obstacle for use in clinical practice.

Delayed-enhancement magnetic resonance imaging (DE-MRI) [25] provides a less invasive alternative for imaging of the scar tissue. The underlying idea is to inject a contrast agent called gadolinium into the subject's bloodstream before acquiring a MR image with a special pulse sequence. The intensity of any scarred tissue is enhanced because the contrast agent takes more time to wash out of the scar tissue than out of normal healthy tissue. In clinical practice, DE-MRI images are commonly obtained by simply waiting after the original acquisition of gadolinium enhanced magnetic resonance angiography (MRA) images, without the need for a second contrast agent injection. In [31], electroanatomic maps and DE-MRI images from corresponding subjects were registered to each other to validate that these two image modalities carry similar information about the location and extent of the ablation scars. This work demonstrated that DE-MRI images offer a viable replacement for the much more invasive electroanatomic mapping for ablation scar visualization.

Atrial ablation scars were segmented in DE-MRI images in [26]. The scar boundary was delineated almost entirely manually, only making use of simple processing methods such as intensity thresholding in manually selected regions of interest. The authors also validated their results by comparing the scar segmentations to electroanatomic maps of matching subjects and found that the majority of the scar tissue was detected. The errors were caused by the low overall quality of DE-MRI images. Similarly, a comparison of scar segmentations in DE-MRI images to the ablation locations recorded during the procedure demonstrated the promise of DE-MRI for ablation scar visualization [19]. To the best of our knowledge, this work represents state-of-the-art for visualization of atrial ablation scars.

Infarction scar segmentation in the left ventricle is a related problem that has received more attention. One approach to solving this problem is to use a pipeline of steps which include different types of thresholding based both on intensity and certain higher level features, such as the volume mass of the infarct each segmented

voxel belongs to and the distance to the left ventricle wall [16, 17]. The algorithm uses a manual segmentation of the left ventricle walls as input. These methods have been shown to produce accurate results on DE-MRI images in animal models, in this case of dogs. We note however that ventricle scar visualization and analysis presents a much easier problem for two reasons. First, the shape of the left ventricle is simpler and has less anatomical variability across subjects than the left atrium. Moreover, infarcts on the left ventricle wall have considerably greater extent compared to atrial ablation scars.

In [14], the authors discuss the importance of ablating only as much heart tissue as is necessary. They explain that if enough atrial cardiac tissue is ablated in a patient, their heart will simply become unable to sustain atrial fibrillation. To date, it has not been conclusively shown whether it is the ablation of specific locations or just the mere ablation of a large enough mass of cardiac tissue that cures atrial fibrillation. It is clear that an automated method for cardiac ablation scar visualization will enable better understanding of the reasons for different outcomes in ablation procedures.

# Chapter 3

## Registration

### 3.1 Background

In medical image analysis, we are often faced with the task of registering, or aligning, two different images. Throughout this thesis, we use several types of registration algorithms for different situations. These can be separated into two categories. In rigid and affine registration methods, the deformation is modeled as a linear transformation followed by a translation. Non-rigid registration methods on the other hand allow much more freedom in the modeling of the deformation. This section describes these two classes of algorithms in more detail, and then focuses on a specific type of non-rigid registration algorithms called demons registration. These algorithms are a central part of our work. We conclude with a discussion of groupwise registration, which is a method for aligning more than two images simultaneously.

#### 3.1.1 Rigid and Affine Registration

Rigid and affine registration algorithms are commonly used in two situations: either as a first step before non-rigid registration when the images are initially considerably misaligned or by themselves when a simple model for the transformation is enough to capture the misalignment between the images. An affine transformation can be modeled as a linear transformation followed by a translation:

$$\mathbf{x}_{\text{out}} = A\mathbf{x}_{\text{in}} + \mathbf{b}, \quad (3.1)$$

and more specifically, in 3 dimensions,

$$\begin{bmatrix} x_{\text{out},x} \\ x_{\text{out},y} \\ x_{\text{out},z} \end{bmatrix} = \begin{bmatrix} a_{11} & a_{12} & a_{13} \\ a_{21} & a_{22} & a_{23} \\ a_{31} & a_{32} & a_{33} \end{bmatrix} \begin{bmatrix} x_{\text{in},x} \\ x_{\text{in},y} \\ x_{\text{in},z} \end{bmatrix} + \begin{bmatrix} b_x \\ b_y \\ b_z \end{bmatrix}. \quad (3.2)$$

This equation transforms the input coordinate space  $\mathbf{x}_{\text{in}}$  to the transformed space  $\mathbf{x}_{\text{out}}$ . Geometrically, affine transformations include rotations, scalings, shears, reflections and translations.

Rigid transformations are a subset of the broader class of affine transformations. They are also defined by Eq. (3.1), but  $A$  is restricted to be an orthogonal matrix, meaning that its columns form an orthonormal basis, with a determinant equal to 1. This constrains the resulting transformation to be composed of solely rotations and translations.

The registration problem can be reduced to optimizing a similarity function between the fixed image  $I_F$  and the transformed moving image  $I_M \circ \Phi$  with respect to the deformation  $\Phi$ :

$$E(\Phi; I_F, I_M) = \text{Sim}(I_F, I_M \circ \Phi). \quad (3.3)$$

There are many possible choices for the similarity function. A simple one that is often used is the sum-squared difference between the intensities of the two images:

$$\text{Sim}(I_F, I_M \circ \Phi) = \|I_F - I_M \circ \Phi\|^2. \quad (3.4)$$

This metric however performs poorly when the images are of different modalities or if for any other reason they have different intensity distributions. For this reason, a popular alternative is to instead maximize the mutual information [35], which measures the statistical dependence between the intensities of the two images. In other words, this measure indicates how much information the intensity values of one im-

age provide about those of the second image. Unlike sum-of-squared differences, the mutual information does not require voxels of similar intensity to be aligned. Instead, it is maximized when the joint distribution of intensities in two images is sharp, or in other words when certain pairs of intensities are consistently aligned with each other over the entire images. Mutual information is expressed in terms of the entropies of the intensity distributions:

$$I(I_F, I_M \circ \Phi) = H(I_F) - H(I_F | I_M \circ \Phi). \quad (3.5)$$

In this thesis, we make use of rigid and affine registration algorithms using a mutual information metric because the images we deal with either have slightly different intensity distributions or are of different modalities altogether. For finer alignment, we use non-rigid registration methods. We review these in the following sections.

### 3.1.2 Non-Rigid Registration

In this work, we use non-rigid registration as part of the segmentation procedure. The vast majority of non-rigid registration algorithms are mathematically described as minimizing a cost function of the following form:

$$E(\Phi; I_F, I_M) = \frac{1}{\sigma_i^2} \text{Sim}(I_F, I_M \circ \Phi) + \frac{1}{\sigma_T^2} \text{Reg}(\Phi), \quad (3.6)$$

where  $I_F$  and  $I_M$  are the fixed and moving images being registered,  $\text{Sim}(I_F, I_M \circ \Phi)$  is a similarity function that is minimized when  $I_F$  and  $I_M \circ \Phi$  are aligned, and  $\text{Reg}(\Phi)$  is a regularization term that encourages certain types of deformations  $\Phi$ . The goal is to minimize this function with respect to the deformation  $\Phi$ .

Registration algorithms are usually characterized by how they model deformations. One approach is to parametrize a free-form deformation via B-splines [27]. The main idea is to represent the non-rigid deformation with a mesh of control points. Each control point is effectively a coefficient assigned to a polynomial function of finite support. The overall deformation is a linear combination of the polynomial basis functions with the corresponding coefficients.

Another type of registration algorithms are fluid based methods [5]. These techniques regularize the registration problem by using equations which describe the motion of a viscous fluid to model the deformation. This sets a hard constraint on the possible deformations  $\Phi$ .

Demons methods [32] represent yet another type of registration algorithms. These are based on computing incremental update deformation fields using optical flow equations and then smoothing them to minimize the regularization term. This type of algorithm is presented in more detail in the next section since it is the one we choose to employ in this work. It is interesting to note that even though the theoretical frameworks for the methods described in this section are different, demons registration methods are actually an approximation to fluid based registration algorithms [3].

As is the case for rigid and affine registration, there are numerous possible choices for the similarity measure  $\text{Sim}(I_F, I_M \circ \Phi)$ . B-splines free-form deformation and fluid based algorithms can use a sum-squared difference metric, but the majority of the implementations opt for the mutual information metric instead due to its increased robustness and accuracy in most situations. On the other hand, demons based registration algorithms have only been demonstrated with the sum-squared difference metric.

There are two main approaches to regularize the optimization problem by restricting the class of possible deformations. The most common one encourages a deformation  $\Phi$  that is in some sense smooth. That is the approach taken by B-splines and demons based registration algorithms. An example regularization term is one that penalizes the second derivatives of the deformation field, and in 3 dimensions can be expressed as follows [27]:

$$\begin{aligned} \text{Reg}(\Phi) = \int_x \int_y \int_z & \left[ \left( \frac{\partial^2 \Phi}{\partial x^2} \right)^2 + \left( \frac{\partial^2 \Phi}{\partial y^2} \right)^2 + \left( \frac{\partial^2 \Phi}{\partial z^2} \right)^2 \right. \\ & \left. + 2 \left( \frac{\partial^2 \Phi}{\partial xy} \right)^2 + 2 \left( \frac{\partial^2 \Phi}{\partial xz} \right)^2 + 2 \left( \frac{\partial^2 \Phi}{\partial yz} \right)^2 \right] dx dy dz. \end{aligned} \quad (3.7)$$

Another common method is to model deformations in a way that intrinsically restricts the set of allowable deformations. Fluid based registration algorithms are an example of this approach since the fluid equations at the core of the algorithm can only represent a particular set of deformations.

### 3.1.3 Demons Registration Algorithm

We choose to work with the symmetric log-domain variant of the demons algorithm because of the combination of its speed and registration accuracy.

This algorithm belongs to the class of demons registration algorithms, first described by Thirion in [32]. It introduces an auxiliary deformation  $s$  and minimizes iteratively the following cost function:

$$E(\Phi, s; I_F, I_M) = \frac{1}{\sigma_i^2} \text{Sim}(I_F, I_M \circ \Phi) + \frac{1}{\sigma_c^2} \text{dist}(\Phi, s) + \frac{1}{\sigma_T^2} \text{Reg}(s), \quad (3.8)$$

where  $\text{Sim}(I_F, I_M \circ \Phi) = \|I_F - I_M \circ \Phi\|^2$  is the measure of image agreement,  $\text{dist}(\Phi, s) = \|\Phi - s\|^2$  is the measure of similarity between the deformations  $\Phi$  and  $s$ ,  $\text{Reg}(s)$  is a regularization term that encourages smoothness in the deformation  $s$ , and the constants  $\{\sigma_i^2, \sigma_c^2, \sigma_T^2\}$  determine the tradeoff between the three terms. This approach creates a decoupled problem solved by alternating between optimizing two different cost functions. We first compute a deformation  $u$  which minimizes

$$E_{\text{add}}(\Phi, u; I_F, I_M) = \text{Sim}(I_F, I_M \circ (\Phi + u)) + \|u\|^2, \quad (3.9)$$

then apply a Gaussian smoothing filter to the updated deformation to satisfy the regularization term.

This method has been further improved by performing the updates of the deformation field at every iteration entirely in the log-domain [33]. More specifically, the warp  $\Phi$  is represented with a smooth and stationary velocity field  $v$  using a one-parameter subgroup of diffeomorphisms [1]. The relationship between the two is then formalized as  $\Phi(x) = \exp(v)(x)$ , meaning that the flow of the velocity field at time one is equal to its equivalent deformation. This parametrization guarantees a diffeo-

morphic deformation and offers the additional advantages of computational efficiency and convenient access to the inverse deformation  $\Phi^{-1}(x) = \exp(-v)(x)$ . In the diffeomorphic log-domain demons, the following energy function is minimized in each iteration [33]:

$$E_{\text{diffeo}}(\Phi, u; I_F, I_M) = \text{Sim}(I_F, I_M \circ \Phi \circ \exp(u)) + \|u\|^2, \quad (3.10)$$

where now  $u$  is the velocity field that defines the incremental update deformation field. The full symmetric log-domain demons registration algorithm proceeds as follows:

---

**Algorithm 1** Symmetric Log-Domain Demons Registration Algorithm

---

**for** number of iterations **do**  
  compute forward demons update  $u^{\text{forw}}$  to minimize  $E_{\text{diffeo}}(\exp(v), u^{\text{forw}}; I_F, I_M)$   
  compute reverse demons update  $u^{\text{back}}$  to minimize  $E_{\text{diffeo}}(\exp(-v), u^{\text{back}}; I_M, I_F)$   
   $u \leftarrow \frac{1}{2}K \star (u^{\text{forw}} - u^{\text{back}})$ , where  $K$  is a Gaussian convolution kernel  
   $v \leftarrow (v + u + \frac{1}{2}[v, u])$ , where  $[v, u]$  represents the Lie bracket  
**end for**

---

The Lie bracket used in the algorithm is defined as:

$$[v, u](x) = |J^v(x)| \cdot u(x) - |J^u(x)| \cdot v(x), \quad (3.11)$$

where  $J^v(x)$  is the Jacobian of the velocity field  $v$  at voxel  $x$  and  $|\cdot|$  is the determinant operator.

Different optimizers for computing  $u^{\text{forw}}$  and  $u^{\text{back}}$  yield slightly different results. Here we use the updates described in [9]:

$$u(x) = \frac{I_F(x) - (I_M \circ \exp(v))(x)}{\|G(x)\|^2 + \frac{\sigma_i^2(x)}{\sigma_c^2}} G(x), \quad (3.12)$$

where  $x$  is a voxel in the image,  $\sigma_i(x)$  is estimated from the image noise,  $\sigma_c$  controls the maximum step length and  $G(x) = -\frac{1}{2}(\nabla_x I_F + \nabla_x(I_M \circ \exp(v)))$  is the symmetric image gradient evaluated using both images.

### 3.1.4 Groupwise Registration

At times it is necessary to register a whole set of images to each other. This process is called groupwise registration and can be useful in several situations, such as for example when we need to summarize the information contained in multiple images. We will discuss such construction in more detail in Chapter 4 in the context of atlas-based segmentation algorithms.

A simple way of aligning multiple images is to define the common coordinate space by choosing a subject out of the image set and aligning all the other images to it. However, this approach clearly introduces a bias towards the initially chosen subject.

A more sophisticated method is to register all of the subjects to a common space which is average in some sense. One such definition is a space such that the concatenation of the deformations of each subject is equal to the identity deformation:

$$\Phi_1 \circ \Phi_2 \circ \dots \circ \Phi_N = Id. \quad (3.13)$$

This definition also leads to a relatively simple iterative algorithm that operates in the log-domain, with the deformations represented as stationary velocity fields. Specifically, the concatenation of two or more small deformations can be approximated by the sum of their corresponding velocity fields [2]:

$$\Phi_1 \circ \Phi_2 \circ \dots \circ \Phi_N \approx \exp \left( \sum_{i=1}^N v_i \right), \quad (3.14)$$

where  $\Phi_i = \exp(v_i)$ . Using this approximation, the condition in Eq. (3.13) can be written as:

$$\sum_{i=1}^N v_i = 0. \quad (3.15)$$

Algorithm 2 below performs groupwise image registration by iteratively computing an average template image and registering the set of images to this template.

The output of this algorithm consists of the set of deformations  $\{\Phi_i\}$  of each image to the common coordinate space and the final average  $\bar{I}$ . We will show in Section 4.1.1

---

**Algorithm 2** Groupwise Registration to Average Space

---

```
compute initial template image  $\bar{I}$  by averaging all images  $I_i$ 
repeat
  for each image  $I_i$  do
    register  $I_i$  to  $\bar{I}$  to obtain deformation  $\Phi_i = \exp(v_i)$ 
  end for
  compute average of velocity fields  $\bar{v} = \frac{1}{N} \sum_{i=1}^N v_i$ 
  for each image  $I_i$  do
    compute unbiased deformation  $\Phi'_i = \exp(v_i - \bar{v})$ 
  end for
  compute new template image  $\bar{I}$  by averaging all images  $I_i \circ \Phi'_i$ 
until convergence to a stable template image  $\bar{I}$ 
```

---

how this groupwise alignment can be used to summarize an image set by forming a parametric atlas.

## 3.2 Intersubject Registration

The general idea behind the segmentation algorithms we will present in Chapter 4 is to transfer information from a set of example segmentations to a new previously unseen image. To accomplish this, we need to align pairs of images of different subjects to each other. In this section, we discuss methods for registering MRA images that we will use for left atrium delineation in Section 4.2.

For the registration experiments we present in this section, we use a set of 16 electro-cardiogram gated (0.2 mmol/kg) Gadolinium-DTPA contrast-enhanced MRA images (CIDA sequence, TR=4.3ms, TE=2.0ms,  $\theta=40^\circ$ , in-plane resolution varying from 0.51mm to 0.68mm, slice thickness varying from 1.2mm to 1.7mm,  $\pm 80$  kHz bandwidth, atrial diastolic ECG timing to counteract considerable volume changes of the left atrium).

### 3.2.1 Methodology

Since the original MRA images of different subjects have large misalignments because of their variable position in the scanner, as well as significant differences in chest

and internal organ sizes, we use an affine registration algorithm with the mutual information cost function [35] as a first step to aligning the images.

The affine registration however only coarsely aligns large structures such as the heart chambers and aorta. Substantial registration errors are present in crucial areas around both the bodies of the heart chambers and the vessels connected to them. To improve image alignment across subjects, we apply a non-rigid registration algorithm. We experimented with several algorithms described in Section 3.1.2 and obtained the best results by employing the symmetric log-domain diffeomorphic demons algorithm [9, 33], which we use throughout this work.

We evaluated the performance of the algorithms qualitatively by examining the overlap of the heart chambers, especially the left atrium, and surrounding vessels in the registered images. We omit the comparison of different registration algorithms in this thesis as the demons registration algorithm produced drastically better results than the alternatives.

One important drawback of demons-based registration algorithms is its use of the sum-squared difference between the intensities of the two images as a measure of similarity. The issue with this approach is that the intensity distributions of the images we are aligning are not necessarily identical. This is especially the case in contrast enhanced images because the contrast agent does not wash out at the same rate in different patients. It is thus necessary to normalize the intensity distributions in the two images in some way before using a sum-squared difference based registration algorithm.

Histogram intensity matching is one approach to performing intensity equalization. We used it as a pre-processing step on the images before performing demons registration when evaluating the different registration algorithms. This algorithm works by finding several key values in the intensity histogram of each image. The key intensities of the moving image are then matched to those of the fixed one. All of the other intensity values in the moving image are computed by interpolating between the matched key values. While this method performed very well for certain pairs of images, it also failed completely for others. One of the problems with histogram

matching is that it requires the two images being matched to have a similar distribution of intensities. This is clearly problematic when the images encompass different fields of view or have different dimensions. In some cases when these properties are the same in both images, their intensity histograms can still have considerably different shapes, causing histogram matching to fail.

To address this problem, we modified the log-domain diffeomorphic demons algorithm to estimate an intensity transformation function between the two images at each iteration. We define a polynomial intensity transformation of the moving image:

$$\tilde{I}_M(x) = \sum_{k=1}^K \theta_k b_k(I_M(x)) = B(I_M(x)) \theta, \quad (3.16)$$

where  $\{b_1(\cdot) \dots b_K(\cdot)\}$  is a set of basis functions and  $\theta = \{\theta_1 \dots \theta_K\}$  is a vector of corresponding coefficients. This transformation effectively modifies the energy function we are optimizing:

$$E(\Phi, u; I_F, I_M) = \|I_F - B[I_M \circ \Phi \circ \exp(u)] \theta\|^2 + \|u\|^2. \quad (3.17)$$

Similarly to the method presented in [13], we use polynomial basis functions up to degree  $K$ . For a fixed velocity field  $u$ , it is easy to see that Eq. (3.17) reduces to a standard linear least squares problem. We thus estimate the coefficients  $\{\theta_k\}$  using the least squares estimate:

$$\hat{\theta} = (A^T A)^{-1} A^T \tilde{I}_F, \quad (3.18)$$

where  $\tilde{I}_F$  is the fixed image reshaped into a vector and  $A$  is defined as follows:

$$A = \begin{bmatrix} 1 & (I_M \circ \Phi)(1) & [(I_M \circ \Phi)(1)]^2 & \dots & [(I_M \circ \Phi)(1)]^K \\ 1 & (I_M \circ \Phi)(2) & [(I_M \circ \Phi)(2)]^2 & \dots & [(I_M \circ \Phi)(2)]^K \\ \vdots & \vdots & \vdots & \ddots & \vdots \\ 1 & (I_M \circ \Phi)(\mathcal{X}) & [(I_M \circ \Phi)(\mathcal{X})]^2 & \dots & [(I_M \circ \Phi)(\mathcal{X})]^K \end{bmatrix}, \quad (3.19)$$

where  $(I_M \circ \Phi)(x)$  is the intensity value of voxel  $x$  in the moving image warped by the current cumulative deformation and  $\mathcal{X}$  is the total number of voxels in the fixed image.

The quality of the registration at a particular iteration affects the estimates of the intensity transformation function. A significant misalignment causes some of the corresponding voxel pairs in the two images to push towards an erroneous estimate. Since we work with images of the same modality, we can assume that the misaligned voxel pairs will have large differences in their intensities. We thus treat such voxel pairs with an intensity difference larger than a certain threshold as outliers and ignore them when computing the new estimates in Eq. (3.18). We determined empirically that setting this threshold to the intensity mean of the fixed image works well in our dataset.

### 3.2.2 Implementation

For the affine registration, we use an ITK implementation [18] with stochastic subsampling, meaning that a random subset of voxels of the image is used to compute the mutual information metric at each iteration. This greatly reduces the time needed for the registration while having little effect on the final alignment.

For the non-rigid registration, we modified a multi-resolution ITK implementation of the symmetric log-domain diffeomorphic demons algorithm [9] to perform intensity equalization as described above. In our implementation, we alternate between estimating coefficients  $\{\theta_k\}$  from corresponding voxel pairs in  $I_M \circ \Phi$  and  $I_F$  using linear least squares with outlier detection as explained above and performing the standard demons iteration described in Algorithm 1.

### 3.2.3 Results

After exploring the parameter space of the registration algorithms to find their optimal values, we constructed a registration pipeline composed of the affine and non-rigid demons registrations. Fig. 3-1 shows the registration results in the form of checker-

board mosaics for one pair of subjects after only affine registration, then after applying the non-rigid log-domain diffeomorphic demons registration algorithm. Checkerboard mosaics consist of alternating square patches from two images and are especially useful for visually evaluating how well structure boundaries in the images align. In our case, the mosaics demonstrate that the non-rigid registration step is essential and yields an accurate alignment of MRA images of different subjects.

In addition, we evaluate the quality of the registration step by quantifying the volume overlap between the left atria in the two aligned images. We use the Dice overlap score [8], which quantifies the overlap between any two label maps:

$$Dice(A, B) = 2 \frac{|A \cap B|}{|A| + |B|}, \quad (3.20)$$

where A and B are regions corresponding to the same label in the two images. Dice scores vary from 0 to 1, with 1 corresponding to perfect overlap. In our case, we use the Dice score to quantify the overlap between expert manual segmentations of the left atrium in the two images. In the moving image, we apply the transformation obtained in the registration step to the manual segmentation before computing the Dice score.

Fig. 3-2 reports the Dice overlap scores of the left atrium resulting from picking one subject from our dataset as the fixed image and registering the remaining 15 subjects to it. We see that in all cases, both the affine and non-rigid registrations significantly improve the Dice score. Additionally, using non-rigid diffeomorphic demons registration after the affine step usually yields a better alignment than simply running the affine registration by itself. This is however not always the case, as we observe that in a few subjects the overlap decreases after non-rigid registration. Instead of modifying and fine tuning the registration algorithms to improve the registration accuracy, we choose to handle these inevitable registration errors directly in the segmentation algorithm. Chapter 4 presents the process by which we avoid using information from misregistered subjects by effectively discarding them.

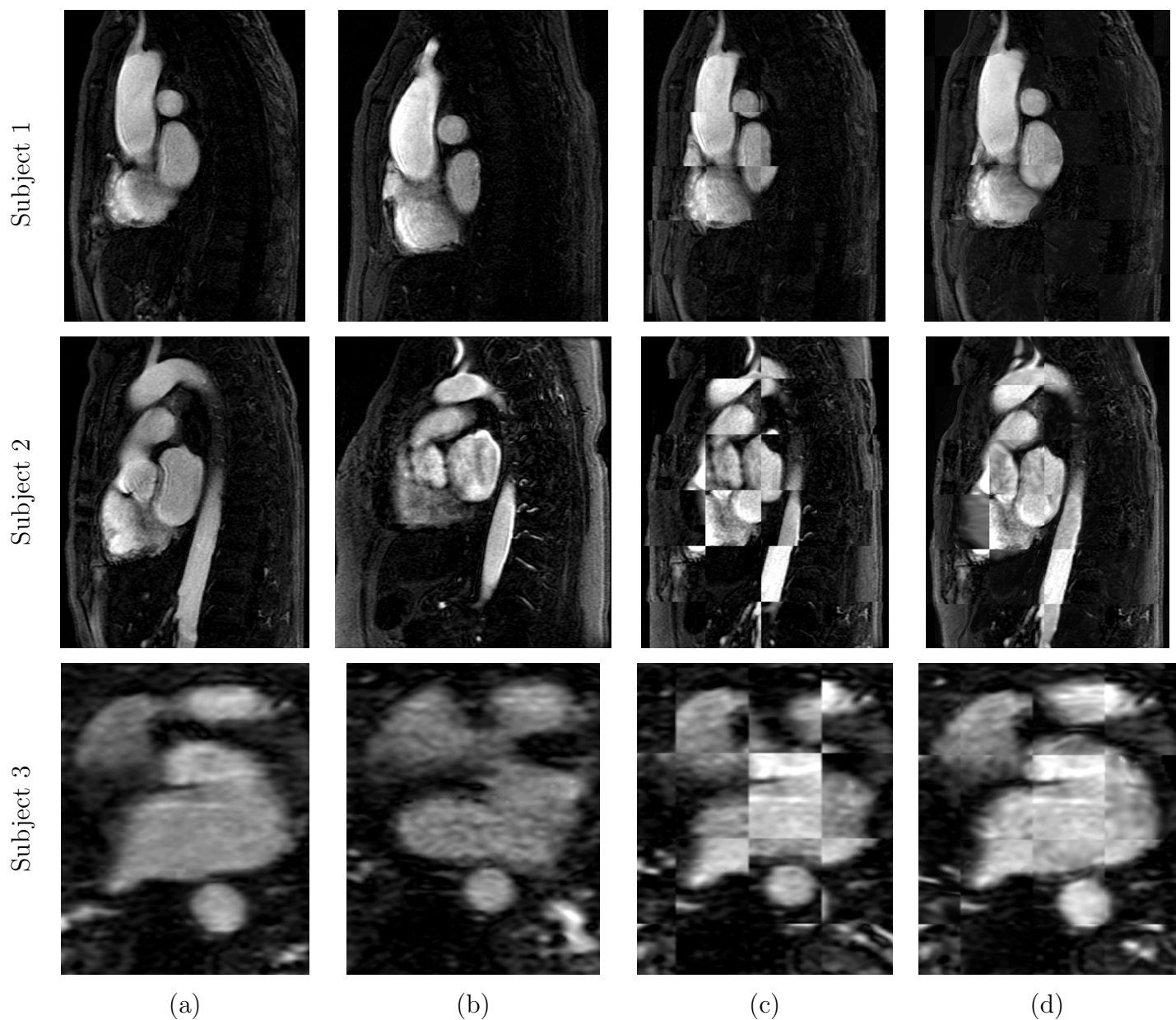


Figure 3-1: Registration results for three different subject pairs. Shown are (a) fixed and (b) moving MRA images, as well as checkerboard mosaics showing registration results after (c) affine and (d) non-rigid diffeomorphic demons registration. Sagittal cross sections are shown for subjects 1 and 2. Axial cross sections are shown for subject 3.

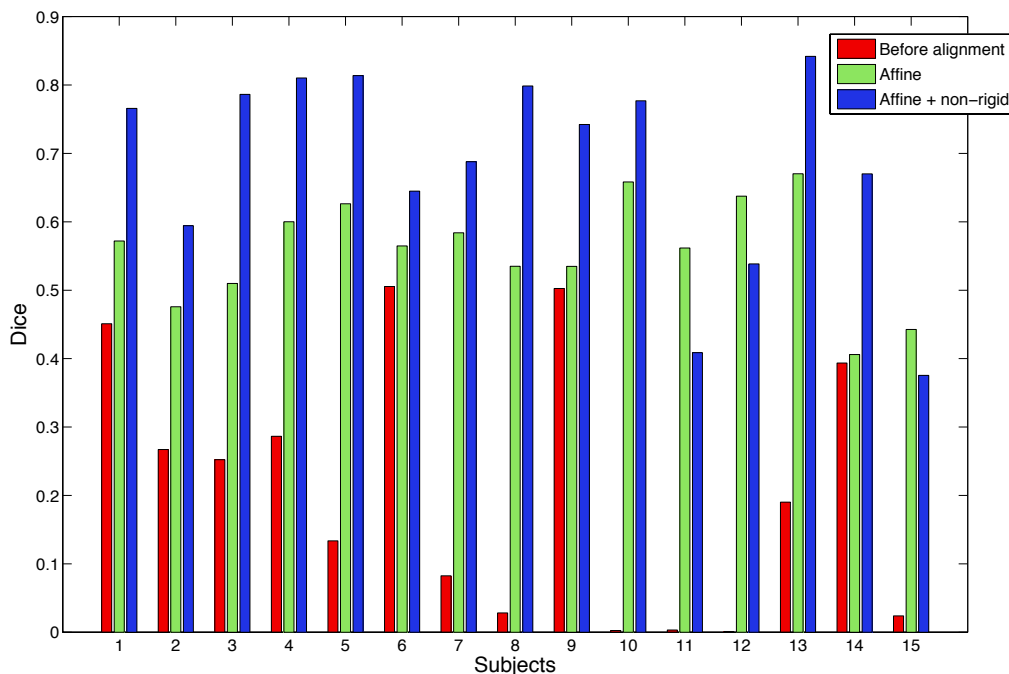


Figure 3-2: Dice overlap scores of the left atrium in 15 pairs of MRA images before alignment (red), after affine registration (green) and after non-rigid registration (blue).

### 3.3 Intermodality Registration

In Chapter 5, we will discuss techniques for the visualization of ablation scars in DE-MRI images. For these, we need to align MRA and DE-MRI images of the same subject in order to transfer information about the location of the left atrium. This is a challenging task because the MRA and DE-MRI images are of different modalities and therefore have completely different intensity distributions.

In this section, we use a dataset that consists of pairs of both MRA and DE-MRI images of 25 patients. The MRA images are electro-cardiogram gated (0.2 mmol/kg) Gadolinium-DTPA contrast-enhanced images. The DE-MRI images are acquired after waiting  $20 \pm 5$  minutes from the original Gadolinium-DTPA injection. They are acquired using a three-dimensional inversion-recovery gradient-echo sequence with electro-cardiogram gating (TR=4.3ms, TE=2.1ms, TI=280ms,  $\theta=15^\circ$ , 150ms end-diastolic ECG timing window). Both modalities have in-plane resolution

varying from 0.59mm to 0.63mm and slice thickness varying from 1.5mm to 2mm.

### 3.3.1 Methodology and Implementation

The MRA and DE-MRI images have drastically different intensity distributions, but since they are acquired without the patient ever leaving the scanner, there is in theory only a slight misalignment which could be modeled by a rigid transformation. However, in reality the heart is also deformed because of its motion and the fact that a different acquisition protocol is used for the two images. We thus apply an affine registration algorithm. We use a mutual information metric [35] to allow the alignment of two images of such highly different modalities. In addition, because of the low contrast and high noise in the DE-MRI images, we use all voxels in the images when computing the mutual information to obtain satisfactory results.

### 3.3.2 Results

Fig. 3-3 illustrates typical results of the affine registration of corresponding MRA and DE-MRI images of the same patient. The first row illustrates a situation where the affine registration considerably improved the alignment between the two images. The areas with the most noticeable improvements on the surface of the left atrium are highlighted by blue arrows. In the second row, the registration produced an overall improvement of the alignment of the left atria of the two subjects, indicated again by blue arrows, but there is an area that remains misaligned after the registration. This area is pointed out by a green arrow. Finally, the third row demonstrates that the affine registration algorithm does not necessarily always improve the alignment of a MRA and DE-MRI image pair. The green arrows highlight this by showing areas that were either already properly aligned before the registration step or contained a small misalignment, and remained practically unchanged by the affine registration.

In this dataset, we do not have expert manual segmentations of the left atrium available to us and consequently we cannot quantitatively evaluate the quality of the alignment.

## 3.4 Summary

In this chapter, we discussed the most common medical image registration algorithms in use today, which included algorithms that allow rigid, affine and non-rigid transformations. We also described in more detail non-rigid demons registration algorithms since these are central to the work in this thesis, before explaining a method for group-wise registration. Finally, we demonstrated the use of these algorithms to register images of different subjects that are of the same modality and pairs of images of the same subject but of different modalities. In the next chapter, we discuss atlas-based segmentation algorithms that function by transferring information between images via registration.

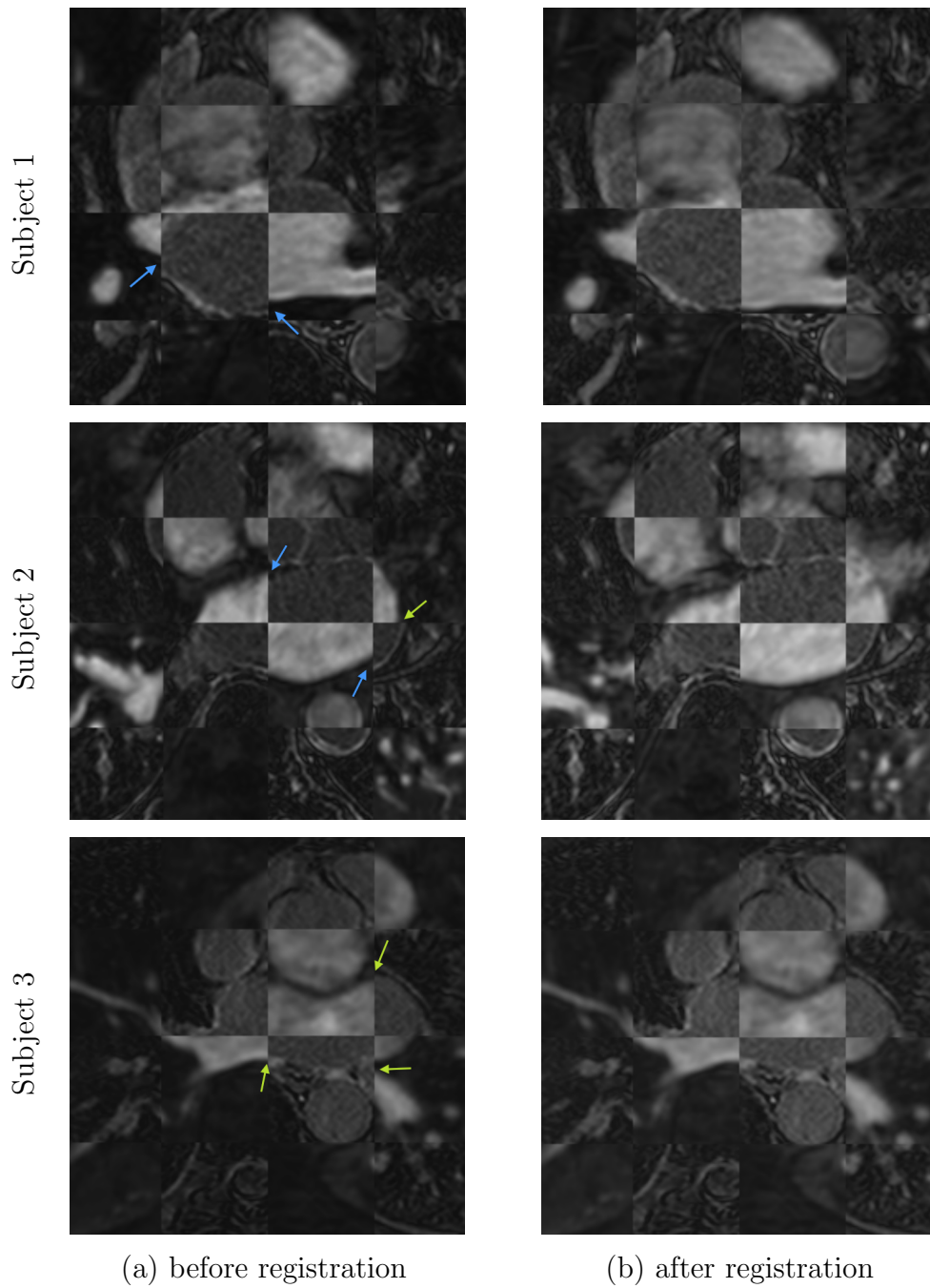


Figure 3-3: Checkerboard mosaics (a) before and (b) after affine registration of MRA and DE-MRI image pairs of three different subjects. Blue arrows show areas on the surface of the left atrium where the alignment considerably improved after affine registration, while green arrows indicate locations where there was little or no improvement.



# Chapter 4

## Atlas-based Segmentation

### 4.1 Background

In this thesis, we present a method for automatically segmenting the left atrium of the heart using atlas-based methods. While atlas-based techniques have traditionally been applied to structures with little anatomical variability, such as the brain, we believe and in later sections demonstrate that they are also applicable to the left atrium, which is a structure with considerable anatomical variability across patients.

The main advantage of atlas-based methods is that they are fully automatic, which is important for our application. In this section, we describe segmentation algorithms based on parametric and nonparametric atlases, which we subsequently use for left atrium segmentation.

#### 4.1.1 Segmentation with Parametric Atlases

The majority of atlas-based segmentation algorithms summarize the training set, composed of images and corresponding example manual segmentations, and then make use of that information to segment a new previously unseen image. This process, called atlas construction, typically creates an intensity template image  $I_{\text{atlas}}$  and a probabilistic label map  $L_{\text{atlas}}$  that together summarize the full training set. This type of atlas is called *parametric* because it reduces the full training set of images and

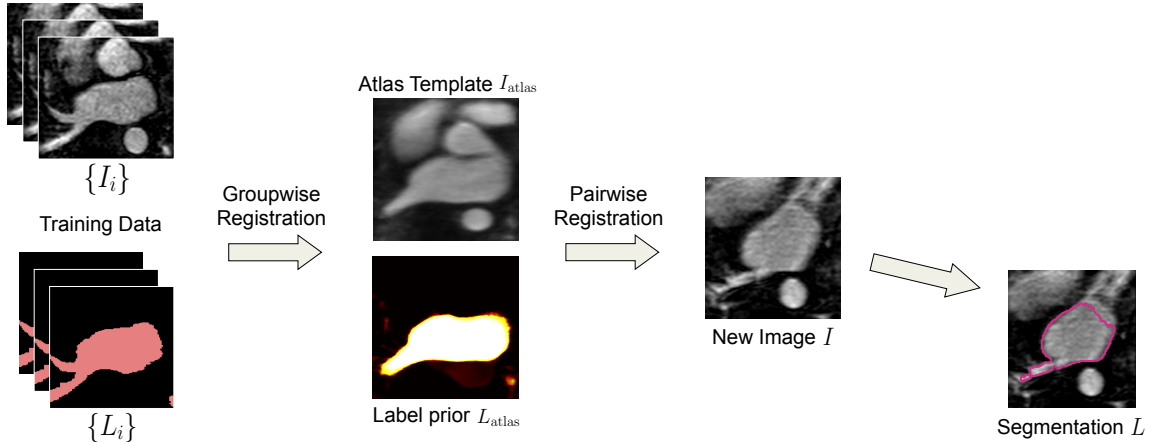


Figure 4-1: Construction and use of a traditional parametric atlas for segmentation.

example manual segmentations to an image template and a corresponding probability map. The template image is used to transfer the information contained in the atlas to the new image via registration. The probabilistic label map on the other hand contains the frequency of occurrence of each segmentation label at every voxel.

Construction and use of such an atlas is illustrated in Fig. 4-1. A set of  $N$  training images  $\{I_i\}$  with corresponding expert manual segmentations  $\{L_i\}$  are first brought into a common coordinate space. These new intensity images and label maps are then averaged to create a template image  $I_{atlas}$  and prior probability map  $L_{atlas}$  respectively. In Section 3.1.4, we described a method for registering all of the training images to each other simultaneously. Once we obtain the set of deformations  $\{\Phi_i\}$  of each training image to a common coordinate space from the groupwise registration algorithm, we form a parametric atlas by applying these to the corresponding manual segmentations  $\{L_i\}$ , then averaging the resulting label maps to compute the probabilistic label map  $L_{atlas}$ . The template image  $I_{atlas}$  is already computed as part of the groupwise registration algorithm.

An example segmentation algorithm that uses such an atlas as a spatial prior is the model-based approach presented in [22, 34]. The authors model the intensities of the voxels belonging to each label class with a Gaussian distribution. The algorithm iterates between solving for the mean and the variance of the Gaussian

distributions, based on the current segmentation, and computing the most likely segmentation given the estimated intensity distributions. The method follows directly from the Expectation-Maximization (EM) algorithm for mixture modeling and for this reason is commonly called EM-segmentation.

While parametric atlas-based segmentation methods have been shown to perform well for segmentation of the brain, they are not necessarily suitable for different applications, such as cardiac segmentation. The problem lies in the high anatomical variability of the heart. Specifically, in the case of the left atrium, the number and locations of the pulmonary veins leaving the atrium body vary across subjects. As a consequence, any misalignment of the veins as they are brought into the same coordinate space before averaging leads to blurry probability maps and templates. Such registration errors are common because of the complexity of the structure and cause the resulting atlas to carry little information about the locations of the pulmonary veins.

### 4.1.2 Segmentation with Nonparametric Atlases

To avoid this considerable drawback, in this thesis we rely on a different class of segmentation algorithms, commonly referred to as label fusion methods. The key idea is to keep the atlas in the form of the original training images  $\{I_i\}$  with their expert manual segmentations  $\{L_i\}$ , instead of summarizing the training set through average statistics. The training intensity images are registered to a new subject while propagating the resulting deformations  $\{\Phi_i\}$  to the label maps, as illustrated in Fig. 4-2. This step produces a collection of label maps in the coordinate space of the new image, which effectively form a subject-specific *nonparametric* atlas. This type of atlas contains much more information than its parametric counterpart we described above. The downside of this method however is that it requires many more registration operations for every new subject we segment. In contrast, parametric atlases only need to be constructed once and a single registration operation is needed for segmentation of a new image.

A nonparametric atlas can be integrated into the segmentation procedure in a

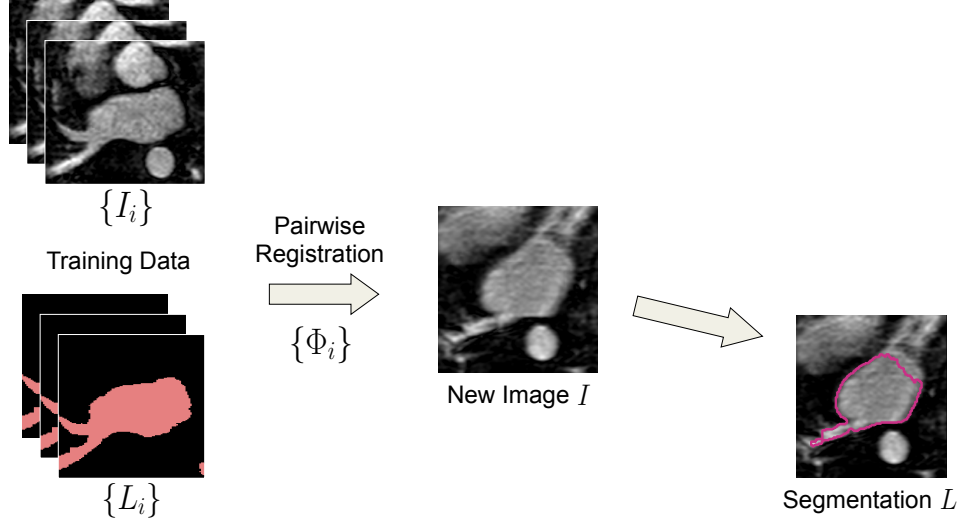


Figure 4-2: Construction and use of a nonparametric atlas for segmentation.

number of ways. One simple option is to use majority voting on the label maps, choosing the most frequent label at each voxel as the final segmentation [15]. This simple method however only makes use of the label maps, completely ignoring the registered training images. An alternative and more involved approach is to use a weighted voting scheme at each voxel, taking into account not only the number of occurrences of each label, but also their locations in the manually segmented structures and the similarity between the intensities of the corresponding voxels in the training and new previously unseen images [29]. Formally, we assume that each voxel of the new image and label map is generated from a single training subject. This is represented by an image  $M$  of the same size as the new image.  $M(x)$  indicates the training image that generated voxel  $x$ . The joint conditional probability of generating a new image  $I$  and its segmentation  $L$  becomes:

$$p(L, I | \{L_i, I_i, \Phi_i\}) = \sum_{\mathcal{M}} p(M) \prod_{x \in \Omega} p(L(x), I(x) | M(x), \{L_i, I_i, \Phi_i\}) \quad (4.1)$$

$$= \sum_{\mathcal{M}} p(M) \prod_{x \in \Omega} p_{M(x)}(L(x), I(x) | L_{M(x)}, I_{M(x)}, \Phi_{M(x)}), \quad (4.2)$$

where  $\Phi_i$  is the warp that brings the training image  $I_i$  into the coordinate space of the

new image  $I$ . The maximum a posteriori (MAP) estimate of the label map provides the segmentation of image  $I$ :

$$\hat{L} = \arg \max_L p(L|I, \{L_i, I_i, \Phi_i\}) = \arg \max_L p(L, I|\{L_i, I_i, \Phi_i\}). \quad (4.3)$$

With the assumption that given the training set, the label at each voxel is generated independently from all other voxels and that  $M$  has a uniform prior, the MAP estimation reduces to an independent decision at each voxel:

$$\hat{L}(x) = \arg \max_{l \in \{1, \dots, \mathcal{L}\}} \sum_{i=1}^N p(L(x) = l, I(x)|L_i, I_i, \Phi_i) \quad (4.4)$$

$$= \arg \max_{l \in \{1, \dots, \mathcal{L}\}} \sum_{i=1}^N p(L(x) = l|L_i, \Phi_i)p(I(x)|I_i, \Phi_i), \quad (4.5)$$

where  $\mathcal{L}$  is the total number of possible labels. Eq. (4.5) assumes that the label and intensity values at each voxel of the new image are conditionally independent given the warp  $\Phi_i$  and the fact that they were generated from training subject  $i$ . This decision rule can be viewed as weighted soft voting with  $p(L(x) = l|L_i, \Phi_i)$  providing the vote and  $p(I(x)|I_i, \Phi_i)$  serving as a weight. The weights are derived from a Gaussian image likelihood:

$$p(I(x)|I_i, \Phi_i) = \frac{1}{\sqrt{2\pi\sigma^2}} e^{-\frac{1}{2\sigma^2}(I(x)-I_i(\Phi_i(x)))^2}, \quad (4.6)$$

where  $I_i(\Phi_i(\cdot))$  is the training image  $I_i$  registered to the new image  $I$ . This term is higher when the two corresponding voxels in the aligned images have similar intensities. The votes are defined through the label likelihood term:

$$p(L(x) = l|L_i, \Phi_i) \propto e^{\rho D_i^l(\Phi_i(x))}, \quad (4.7)$$

where  $D_i^l(\Phi_i(\cdot))$  is the signed Euclidean distance map of the manual segmentation of the training subject  $i$  in the coordinate space of the new subject and  $\rho$  is the slope parameter. This term assigns higher votes to voxels that are inside the structure of

interest and farther from the boundary. A description of the implementation of the full algorithm is shown below.

---

**Algorithm 3** Weighted Voting Label Fusion Segmentation

---

**for** each training subject  $i$  **do**  
  register training image  $I_i$  to new image  $I$  to obtain warp  $\Phi_i$   
  **for** each voxel  $x$  in new image domain  $\Omega$  **do**  
    compute weight  $p(I(x)|I_i, \Phi_i)$  using Eq. (4.6)  
    **for** each possible label  $l \in 1, \dots, \mathcal{L}$  **do**  
      compute unnormalized vote  $p(L(x) = l|L_i, \Phi_i)$  using Eq. (4.7)  
    **end for**  
  **end for**  
**end for**  
normalize votes such that  $\sum_{l=1}^{\mathcal{L}} p(L(x) = l|L_i, \Phi_i) = 1$   
compute segmentation  $\hat{L}$  using Eq. (4.5)

---

In contrast to simple majority voting, this method is called *weighted* voting since it gives more importance to label occurrences in the manual segmentations which have similar voxel intensities as the corresponding new image voxel and are further from the edges of the structure, or in other words, are labeled with more certainty.

## 4.2 Robust Left Atrium Segmentation

### 4.2.1 Methodology

The high anatomical variability of the heart’s left atrium makes its segmentation a particularly difficult problem. Specifically, the shape of the left atrium lumen, as well as the number and locations of the pulmonary veins connecting to it, vary substantially across subjects.

In this thesis, we opt for the nonparametric approach described in the previous section. To align the training images to the new scan, we use our intersubject registration pipeline developed in Section 3.2 that consists of an affine step followed by a non-rigid diffeomorphic demons registration. We then employ the weighted voting label fusion segmentation algorithm [29] described above for the segmentation of the left atria in MRA images [7].

## 4.2.2 Results

For the experiments in this section, we use the same 16 patient MRA dataset we used for our intersubject registration experiments in Section 3.2. We perform leave-one-out experiments by treating one subject as the test image and the remaining 15 images as the training set, and repeating for each subject in the dataset.

### Algorithm Parameters

After registering the training images to the test subject, we use the weighted voting label fusion segmentation algorithm described above to obtain the left atrium segmentation. There are two parameters that need to be set in this segmentation algorithm. The width of the Gaussian distribution  $\sigma$  in the image likelihood term determines how sensitive the vote weights are to differences in intensities between the training and test images. The slope coefficient  $\rho$  multiplies the Euclidean signed distance map in the label likelihood. An increase in  $\rho$  amplifies the importance of the distance of voxels from the boundary of the structure of interest in the votes they provide.

In our experiments, we set these parameters to  $\sigma = 100$  and  $\rho = 1.5$ . We explored the parameter space by varying  $\sigma$  between 50 and 500, and  $\rho$  between 0.3 and 2.5. During this process, we confirmed that our method is in fact robust to the choice of the parameters. The difference between the best and the worst Dice overlap scores obtained between the expert manual and automatic left atrium segmentations for each subject while varying the parameters was  $0.05 \pm 0.03$ . We also explored different values for the polynomial degree of the intensity transformation in the registration algorithm. We varied the degree from 1 to 5 and found that it had similarly little effect on the results, with a  $0.008 \pm 0.007$  difference between the best and worst overlap scores for each subject. We choose a degree of 3 because it provided the highest overall Dice scores. While we did need to determine the optimal values of these parameters empirically, this calibration of the algorithm is only necessary once per dataset. The parameters of the method are dependent on broad image characteristics such as the contrast, and they remain stable for images acquired using the same scanner and

acquisition protocol. Therefore, an important advantage of our approach is that no parameters need to be adjusted for each new image.

## Baseline Methods

We compare our method of weighed voting (WV) label fusion to three alternative automatic atlas-based approaches: majority voting (MV) label fusion, parametric atlas thresholding (AT) and atlas-based EM-segmentation (EM). The majority voting label fusion is similar to weighted voting, except it assigns each voxel to the label that occurs most frequently in the registered training set at that voxel. We also construct a parametric atlas that summarizes all 16 subjects in a single template image and a probabilistic label map by performing groupwise registration to an average space as described in Section 4.1.1. After registering this new atlas to the test subject, we segment the left atrium using two different approaches. In atlas thresholding, we simply threshold the warped probabilistic label map at 0.5 to obtain the segmentation. This baseline method is analogous to majority voting in the parametric atlas setting. We also use the parametric atlas as a spatial prior in a traditional model-based EM-segmentation [22]. Note that this construction favors the baseline algorithms as it includes the test image in the registration of all subjects into the common coordinate frame.

## Qualitative Evaluation

In our application, correctly segmenting the pulmonary veins of the left atrium is crucial. Therefore it is important to visually inspect the resulting segmentations to fully evaluate them. Fig. 4-3 shows segmentation outlines of expert manual segmentations and the four methods we compare on corresponding slices of four different subjects.

In the first row, majority voting and atlas thresholding miss a pulmonary vein that is correctly identified by our approach. This is due to the fact that both of these baseline methods weigh the contributions of each training subject equally. The majority of the pairwise registrations between the training and test subjects failed in the area of that pulmonary vein, which caused it to be excluded from the resulting left

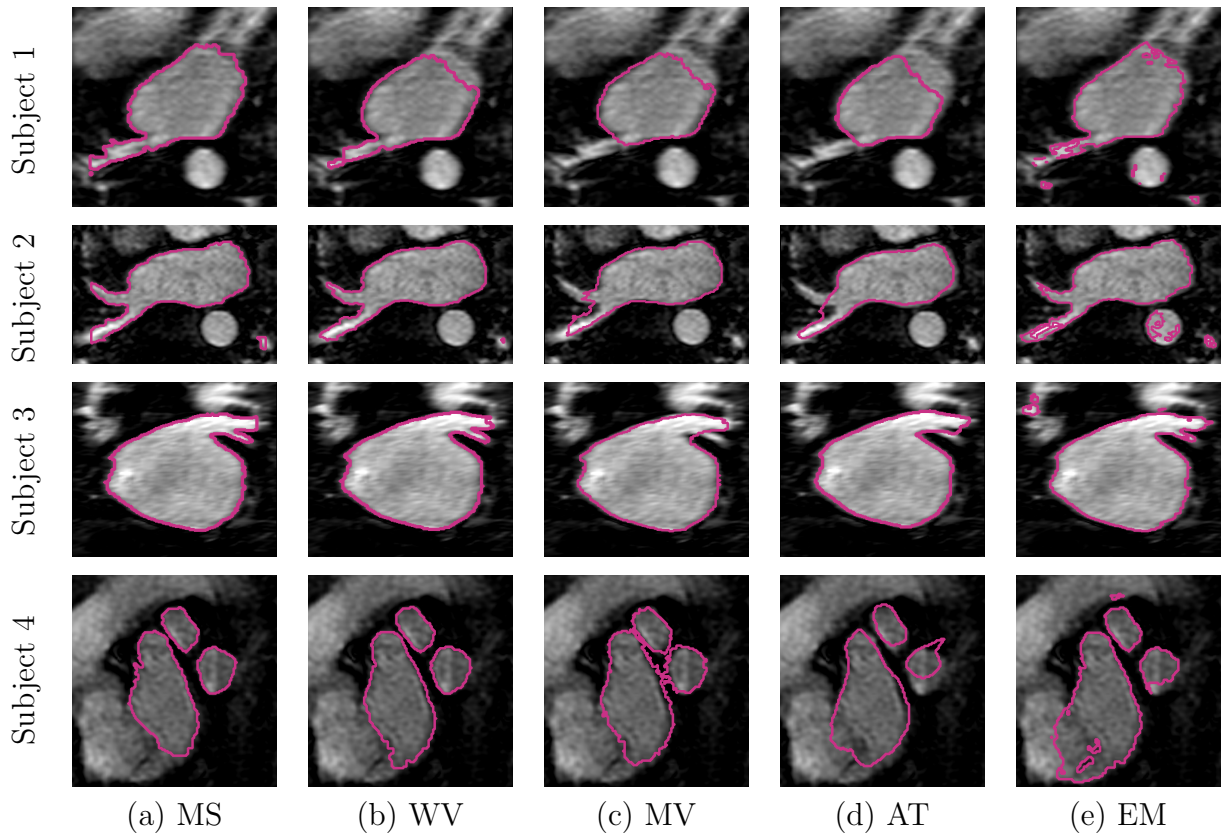


Figure 4-3: Example segmentations of four different subjects: (a) expert manual segmentation (MS), (b) weighted voting label fusion (WV), (c) majority voting label fusion (MV), (d) parametric atlas thresholding (AT) and (e) EM-segmentation using the parametric atlas as a spatial prior (EM).

atrium segmentation. In contrast, in our weighted voting algorithm, it is not necessary for a majority of training subjects to be in agreement in a certain area to be included in the segmentation. Since the contribution of each training image is weighted by the local intensity similarity, the algorithm effectively ignores the misregistered training subjects when computing the segmentation around the pulmonary vein, yielding a correct segmentation. EM-segmentation only partially segments that vein while at the same time producing false positives in the aorta and atrial body. This result is expected since EM-segmentation is a relatively simple intensity based method that segments regions as left atrium if they have high intensity and a non-zero prior, meaning that at least one of the left atria in the training images was mapped to these locations. This method is therefore much less robust since one failed registration can induce significant segmentation errors.

The second and third rows show similar situations. In the last row, all methods correctly segment the pulmonary veins, but our method produces the most accurate outlines. In that situation, the weighted voting label fusion algorithm effectively compensates for small consistent registration errors, which are inevitable at boundaries of complex structures such as the pulmonary veins. The weights based on the local image similarity push the segmentation to better fit sharp intensity changes.

After detailed analysis of all subjects, we conclude that our method is robust to the high anatomical variability of the left atrium as it does not miss a single pulmonary vein in the whole dataset.

Fig. 4-4, we shows 3D renderings of several typical left atrium segmentations obtained using our method, alongside renderings of the expert manual segmentations of the same left atria for comparison. We see that the automatic and manual segmentations are very similar. There are still however some small islands of voxels in our automatic segmentations that appear to be noise. Upon closer inspection, it becomes apparent that the vast majority of them are actually correct segmentations that belong to pulmonary veins. It is the fact that large parts of these extended portions of veins were missed in the segmentations that makes these few correctly labeled voxels stand out. The pulmonary veins are also generally not segmented as far as they are in the manual segmentations. There are two reasons for this. First, it becomes increasingly difficult to correctly register complex and variable structures like veins as their size decreases. Secondly, there is no gold standard on how far to manually segment the pulmonary veins, so different training subjects provide inconsistent information in these areas even if they are registered properly.

## **Quantitative Evaluation**

We also evaluate our results quantitatively by computing the Dice overlap score [8] between the automatic and expert manual segmentations. As a reminder, this measure quantifies the volume overlap between two label maps and varies from 0 to 1, with 1 corresponding to perfect overlap. Fig. 4-5 reports these scores for each method, as well as differences in these scores between our method and the alternatives. To

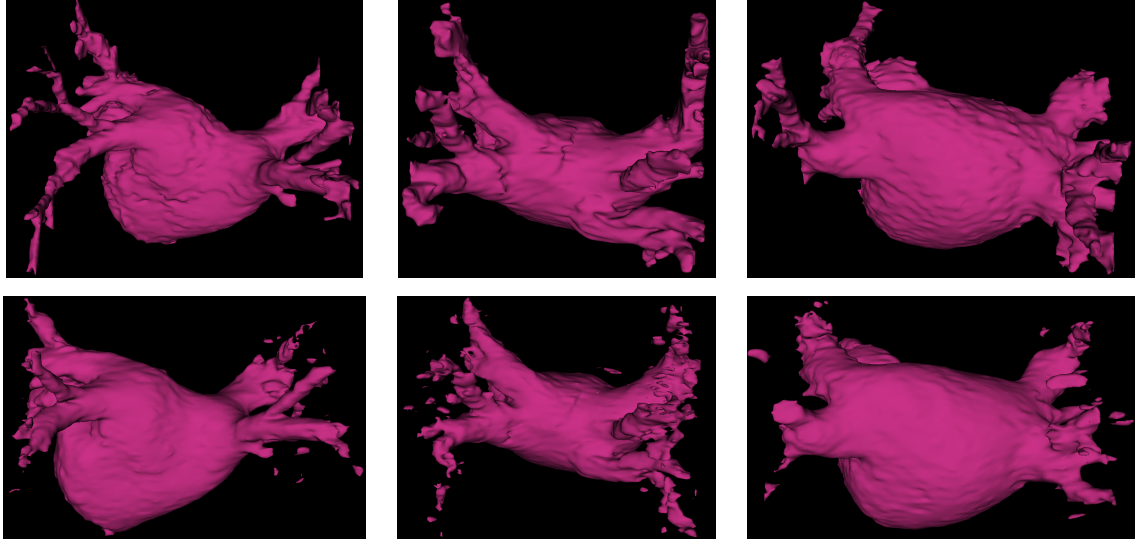


Figure 4-4: Qualitative evaluation of left atrium segmentations in three different subjects. First row shows expert manual segmentations. The corresponding automatic segmentations produced by our method are in the second row.

compute the Dice difference between two methods, we subtract the Dice score of the second method from the score of the first one for each subject. For these differences, we also compute their statistical significance, conveyed by the  $p$ -value, using a single-sided paired  $t$ -test. In this situation, the  $p$ -value represents the probability of seeing differences between results produced by two different methods larger than what we observed, under the hypothesis that the mean of these differences is zero. We compute the  $t$ -statistic corresponding to the single-sided paired  $t$ -test using the following equation:

$$t = \frac{\sum_{i=1}^N (X_i - Y_i)}{\sigma_D \sqrt{N}}, \quad (4.8)$$

where  $X_i$  and  $Y_i$ ,  $i = 1, 2, \dots, N$ , are matching Dice scores for two different methods and  $\sigma_D$  is the standard deviation of the set of differences of these paired scores. The  $p$ -value is computed by subtracting the value of the cumulative probability function of the  $t$ -distribution for this  $t$  from one. In practice, this value is usually looked up in a  $t$ -distribution table.

We also compare the results in the most critical areas by manually isolating the

pulmonary veins in each of the manual and automatic segmentations, and then computing Dice scores only in these critical areas. We observe that our approach consistently outperforms the other methods. We note again that since atlas-based EM-segmentation is an intensity based method, it does relatively well in segmenting pulmonary veins, but suffers from numerous false positives in other areas, which lower its overall Dice scores.

One problem with using Dice scores for measuring the quality of a left atrium segmentation is that they depend on how far the pulmonary veins draining into the atrial body were segmented by the expert. For example, if the manual segmentation for the test subject follows the pulmonary veins far, but the delineations in the training set only include a short segment from the start of the vein, this will cause discrepancies between the automatic and manual segmentations and reduce the overlap between them. Developing evaluation metrics for such situations is an interesting direction to pursue in the future.

## **Computation Time**

Table 4.1 presents the computational cost for all methods. The computation time includes the time needed to perform the registrations and the time required by the segmentation step. All of these experiments were performed on a machine with 8 2.83 GHz cores and 16 GB of RAM. Although our weighted voting label fusion method takes the most amount of time to run, this is mainly due to the numerous pairwise registrations needed to compute the necessary subject-specific parametric atlas. These registrations are completely independent of each other and could thus be computed in parallel. Another way of reducing the computation time could be by only using the most pertinent training subjects for each test subject being segmented, which will reduce the number of pairwise registrations to compute. This interesting direction for future work will be further explored in the final chapter. It is important however to note that for our specific application of segmentation for cardiac ablation procedures, a computation time of several hours still fits within the time constraint since the magnetic resonance angiography scan of the patient is commonly performed

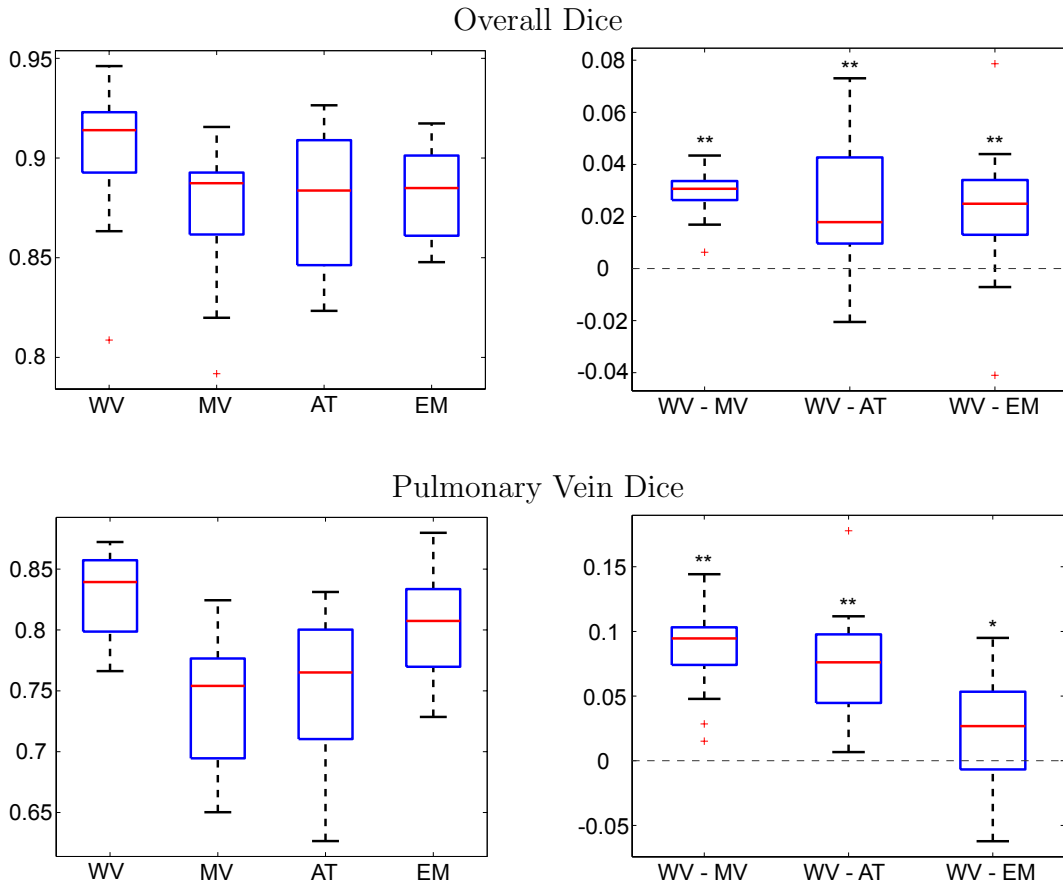


Figure 4-5: Dice scores of results for weighted voting label fusion (WV), majority voting label fusion (MV), parametric atlas thresholding (AT) and atlas-based EM-segmentation (EM). For each box plot, the central red line indicates the median, the boxes extend to the 25<sup>th</sup> and 75<sup>th</sup> percentiles, and the whiskers extend to the most extreme values not considered outliers, which are plotted as red crosses. Stars indicate that the weighted label fusion method achieves significantly more accurate segmentation than the baseline method (single-sided paired t-test, \*:  $p < 0.05$ , \*\*:  $p < 0.01$ ).

Table 4.1: Computation times for different left atrium segmentation methods

Method	Registration	Segmentation	Total
WV	8 min $\times$ 15	5 min	125 min
MV	8 min $\times$ 15	0.5 min	120.5 min
AT	8 min	0.1 min	8.1 min
EM	8 min	15 min	23 min

well before the actual procedure.

### 4.3 Summary

We began this chapter by discussing atlas-based segmentation algorithms. We described two different approaches to this type of segmentation: using parametric and nonparametric atlases. Parametric atlases are formed by summarizing the training set into a single template image and a corresponding probabilistic map. In contrast, nonparametric atlases consist of the training images and expert manual segmentations warped to the coordinate space of the new image being segmented. We presented weighted voting label fusion, a segmentation algorithm that employs a nonparametric atlas to produce a segmentation by combining weighted votes from the training subjects. The weights and votes depend on the local intensity similarity between the training and test images, and the confidence in particular regions of the manual segmentations. Finally, we presented our method for automatically segmenting the left atrium of the heart in MRA images by making use of the weighted voting label fusion algorithm. We demonstrated empirically that our approach outperforms other comparable methods. In the following chapter, we will make use of these left atrium segmentations to visualize cardiac ablation scars from DE-MRI images.

# Chapter 5

## Ablation Scar Visualization

The visualization of cardiac scars resulting from ablation procedures in delayed enhancement magnetic resonance images (DE-MRI) is a very challenging problem. First, these scars are located on the wall of the left atrium, which as we discussed in previous sections is a structure with significant intersubject anatomical variability. Much of the scar volume is concentrated around the interfaces of the left atrium body and the pulmonary veins, which are areas that vary the most across patients. Moreover, each ablation procedure depends on many factors that cause the exact location and shape of the scars to be different in each case. In addition, some tissue on neighboring heart chambers and structures appears enhanced in DE-MRI images even though it is not ablation scar, which could lead to false detections. Visualization is also challenging because even the most advanced acquisition techniques yield DE-MRI images with relatively poor contrast.

### 5.1 Methodology

With all of these difficulties, performing this segmentation without exploiting some prior knowledge or significant feedback from the user is extremely challenging. Most previous attempts to segment scar in DE-MRI images relied heavily on input from the user. In contrast, we avoid this by automatically segmenting the left atrium in the DE-MRI images of the patients. The atrium segmentation provides us with prior

information about the location and shape of the left atrium, which in turn helps counter some of the challenges that were previously solved by requiring significant amounts of user interaction. We obtain this segmentation by first segmenting the left atrium in the MRA image of the patient’s heart using the method presented in Section 4.2. We then align the MRA image to the corresponding DE-MRI image of the same subject as described in Section 3.3. With these two images aligned, we transfer the left atrium segmentation from the MRA to the DE-MRI image by applying the transformation computed in the registration.

In this chapter, we will use both datasets described earlier in the thesis. We use the set of 16 MRA images with expert manual left atrium segmentations as a training set for left atrium segmentation. The second dataset consists of 25 pairs of MRA and DE-MRI images on which we perform our scar visualization experiments. This last dataset however does not include example manual segmentations of the left atrium, which is the reason we use the other dataset as the training set. The MRA images in the two datasets were acquired using different scanning protocols. Consequently, we expect the automatic left atrium segmentations produced for MRA images in the second dataset to contain more imperfections than those presented in Section 4.2 since the training and test images do not come from the same set. In addition, it is clear from the results presented in Section 3.3 that the MRA to DE-MRI registrations are not perfect, leading to additional errors in the transferred segmentation.

For all of these reasons, we need to account for segmentation errors. We assume that the ablation scars are located within a certain distance of the left atrium segmentation. This approach requires us to determine an optimal value for this distance, which effectively is our margin of error. On the one hand, we want the distance to be large enough to counteract errors in the left atrium segmentation. Conversely, reducing the search space in such a way is only useful when the distance is small enough to avoid large portions of neighboring structures that might present false detections.

We decide to find the best value for this distance empirically using expert manual segmentations of the ablation scars. We first segment the left atrium in the MRA images and transfer it to the DE-MRI images as explained above. We then search

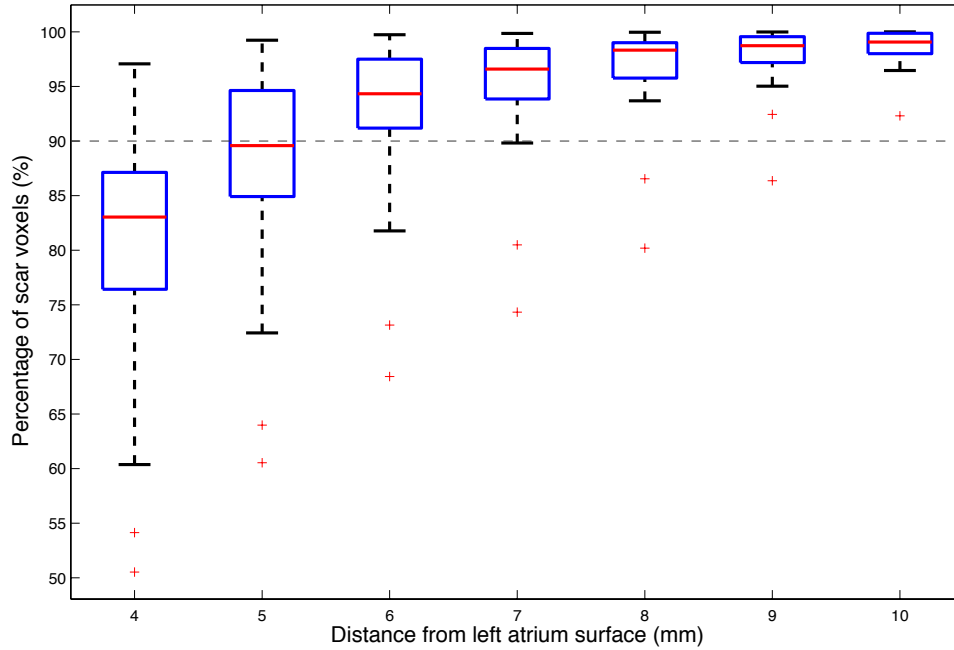


Figure 5-1: Percentages of manually segmented ablation scar voxels that lie within a particular distance of the automatically generated left atrium segmentations in DE-MRI images. Each box plot summarizes the results from 25 subjects; the central red line in each box represents the median, the boxes extend to the 25th and 75th percentiles, and the whiskers extend to the most extreme values not considered outliers, which are plotted as red crosses.

for the smallest band that defines a volume around the segmented left atrium surface that encompasses an acceptable portion of the manually labeled scar voxels. For each value of the band width, we compute the percentage of scar voxels that lie within that distance of the automatically generated left atrium segmentation surface in the DE-MRI image of each subject. Fig. 5-1 shows the results of these experiments for several tested distances.

For the optimal distance, we pick the width of the smallest band that contains 90% of the scar voxels. We decide not to consider the two outlier subjects, plotted as red crosses in Fig 5-1, since they show considerably larger distances from the rest, which is likely due to significant errors in the left atrium segmentation or alignment of MRA and DE-MRI images. Using these guidelines, we select a distance of 7mm

on either side of the atrium surface.

### **Projecting Data Onto Left Atrium Surface**

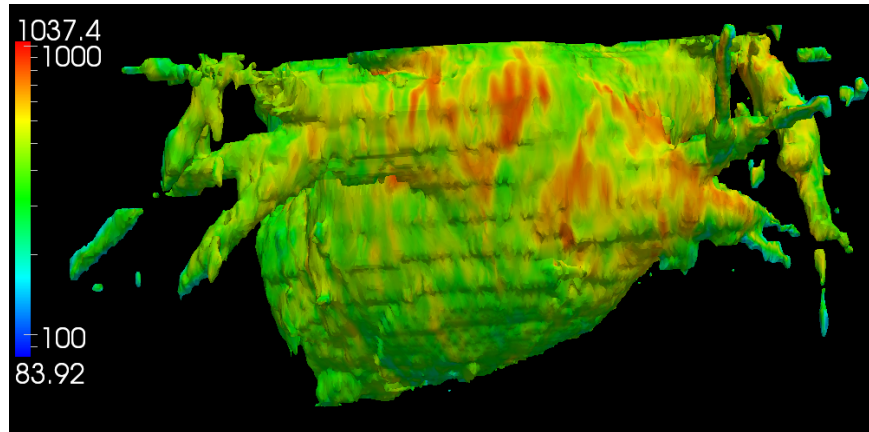
Once we have determined the width of the band to be considered, a simple method for visualizing the ablation scars is to project the DE-MRI data onto the corresponding left atrium surface. We generate this visualization by computing at each vertex of the atrial surface a projection of the DE-MRI image along its normal vector. We build the surface model from the left atrium segmentation using a marching cubes algorithm [23] implemented in 3D Slicer [6]. This model already includes the normals since these are routinely computed before rendering.

We restrict the projection to only use image voxels within the previously determined distance of 7mm of each side of the left atrium surface. Specifically, for each vertex of the surface, we walk along its normal up to a distance of 7mm away from the atrium surface and compute a scalar projection value. We use linear interpolation to compute the intensity values at non-integer image coordinates. We experimented with several different projections and found that a simple maximum intensity projection yields the best results.

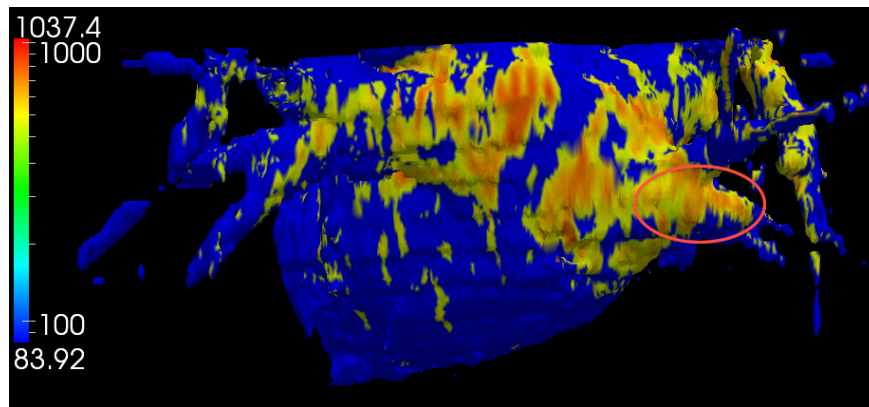
## **5.2 Results**

Fig. 5-2 illustrates the maximum intensity projection results for one subject. In addition, we automatically threshold these projection values by computing the 75th percentile and show the resulting visualization as well. For comparison, we also project the expert manual scar segmentation onto the same left atrium surface.

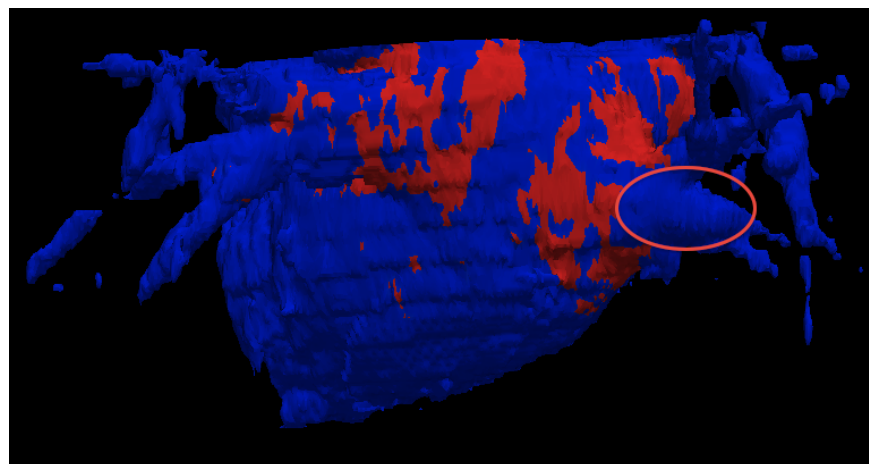
We confirm visually that the thresholded projection values correlate well with the manual scar segmentations. Nevertheless, there is one area, circled in Fig. 5-2, where these two differ considerably. This discrepancy is due to an imaging artifact caused by the acquisition protocol. A pencil beam is used to track large heart motion induced by breathing during the acquisition. This beam also causes some of the tissue on one of the pulmonary veins to appear enhanced in the resulting DE-MRI image. This



(a) Maximum intensity projection of DE-MRI image onto left atrium surface



(b) Maximum intensity projection thresholded at 75th percentile



(c) Projection of expert manual scar segmentation

Figure 5-2: Comparison of projections of DE-MRI data and manual scar segmentation onto left atrium surface. Circled area indicates acquisition artifact that causes non-scar tissue to appear enhanced in the DE-MRI image.

confuses our intensity-based approach and by consequence the thresholded maximum intensity projection erroneously includes this artifact.

We compute Dice overlap scores between the thresholded maximum intensity projections and the manual ablation scar segmentations projected onto the surface. These surface overlap scores are reported in Fig. 5-3. For each subject, we show both the optimal Dice score produced by the best threshold, as well as the score that results from automatically thresholding the maximum intensity projection at its 75th percentile. We conclude that the automatic threshold generally produces results that are similar to those produced by the optimal threshold selection. However, the Dice scores are not very high, with a mean of only 0.45. The relatively low values can be explained in part by the imaging artifacts described earlier. These clearly considerably reduce the overlap score by causing a large portion of one pulmonary vein's surface to be erroneously labeled as scar.

### 5.3 Summary

In this chapter, we described our approach for automatic visualization of cardiac ablation scars in DE-MRI images. The main idea is to take advantage of the fact that ablation scars must be located on the left atrium surface. We first transfer our automatic left atrium segmentation from the MRA to the DE-MRI image of the same patient. We then perform a maximum intensity projection of the DE-MRI image within a certain band of the left atrium surface. This method enables us to compensate for inevitable small segmentation and registration errors. We determined the optimal band width experimentally. Finally, we demonstrated an automatic threshold procedure that results in a visualization which correlates well with the expert manual scar segmentations.

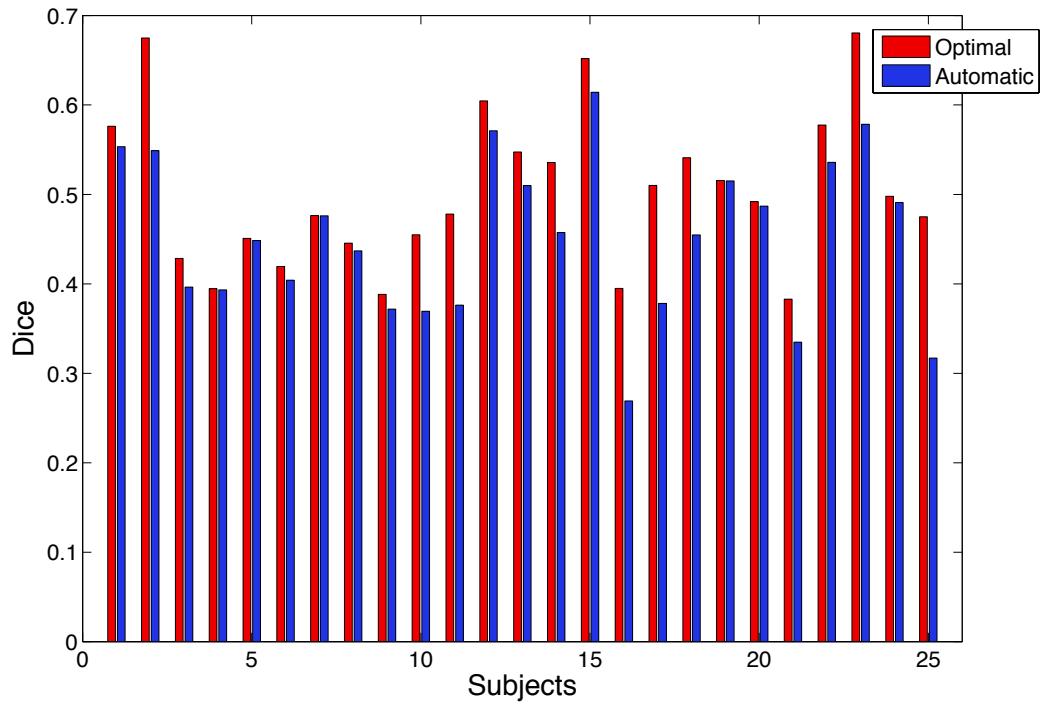


Figure 5-3: Dice overlap scores of the thresholded maximum intensity projections on the surface and the projected manual ablation scar segmentations. Shown in blue are the Dice scores produced when using the automatically determined threshold, while the overlap scores resulting from the optimal thresholds are shown in red.



# Chapter 6

## Discussion and Conclusions

### 6.1 Robust Left Atrium Segmentation

In this thesis, we presented methods for segmentation and visualization in the context of cardiac ablation procedures. We first demonstrated a method for automatically segmenting the left atrium in contrast enhanced magnetic resonance angiography (MRA) images. The resulting segmentations can be used in the planning stages of cardiac ablation surgery. In addition, the segmentation can help to visualize ablation scars resulting from the procedure by providing a spatial prior for the scar location.

High anatomical variability of the left atrium presents a major challenge for robust segmentation. We chose to employ a nonparametric atlas-based method for segmentation. The label fusion approach registers the training set to the new subject image to be segmented and combines weighted votes from training subjects to assign a label to every voxel in the new image. The weighted votes are computed independently at each voxel; they combine the intensity similarity between the training and new images and the voxel's location in the structure of interest. A better agreement of intensity values at a voxel located deeper within the structure translates into larger weights and votes, respectively.

For registration of the training images to the novel scan, we used the symmetric log-domain demons algorithm. To handle global shifts in the intensity distribution across images, we modified this algorithm to perform iterative intensity transforma-

tion during each iteration. We modeled the intensity transformation as a polynomial function of the image intensity values. The intensity equalization improved the registration results. It was also necessary to ensure the segmentation step provided optimal results since the voting weights depend on intensity differences between images.

We compared our method to other automatic approaches using leave-one-out cross-validation. Our experimental results demonstrated that our method successfully handles high anatomical variability, yielding accurate segmentation and detecting all pulmonary veins in all subjects. By explicitly modeling the anatomical variability represented in the training set instead of summarizing it, our method outperformed the baseline techniques.

Qualitatively, the weighted voting segmentation algorithm corrected for small consistent registration errors, which are inevitable in the presence of such high anatomical variability. The weighted voting algorithm counteracted misregistration by discarding votes from training subjects at particular voxels with considerably different intensity values from the new subject image being segmented. Such discrepancies are in nearly all cases caused by small misalignments and thus deemphasizing the misregistered training images in local voting decisions improves the segmentation results.

The increased accuracy came at the cost of additional computational time since each image in the training set needs to be registered to the new subject image. However, this requirement did not pose a problem in our application because the left atrium segmentation does not need to be produced in real-time. The computational time can also be substantially reduced by parallelizing the registration step since all of the necessary pairwise registrations are independent from each other.

### **Future directions**

Since the dataset we used only contained 16 subjects and we performed experiments using leave-one-out cross-validation, where each patient is used in turn as the test subject with all the others forming the corresponding training set, one interesting question is whether or not it was important for the training set to contain several examples similar to the test subject for the segmentation to be successful. We found

that there was no clear relationship between our method’s performance on a specific subject and the number of similar anatomies in the training set. For example, one subject in our dataset had a pulmonary vein that was not present in any of the other patients. Our method still produced an accurate segmentation of that vein, even with no similar left atrium anatomy in the training set.

However, we cannot be sure that this is generally the case without characterizing the anatomical variability of the training set in more detail. An interesting future direction of research would be to describe the variability of the left atrium in the training population by finding sub-groups that contain subjects with similar topology. Similar analysis has been demonstrated on brain images [28]. Developing such methods for cardiac applications would require extension to handle shape and topology differences in populations of structures with much higher anatomical variability.

In addition to providing a better understanding of the topological variations of the left atrium, this type of population clustering could also improve the results of the segmentation algorithm described in this thesis. One could determine the population sub-groups in the training set and match each new subject to one such cluster. Using only this sub-group of most similar subjects as the training set should lead to more accurate segmentation as it will remove some burden from the weighted voting label fusion segmentation algorithm in discarding dissimilar training examples. This approach would also drastically reduce the number of necessary pairwise registrations, which are currently the bottleneck in the algorithm.

Finally, the methods we developed are not specific to the left atrium. It would thus be interesting to see how well the proposed algorithms would perform in application to other structures with high anatomical variability.

## 6.2 Ablation Scar Visualization

We also described methods for automatic visualization of scars resulting from cardiac ablation procedures. This problem has obvious clinical implications since the reasons for different outcomes of the ablation are not yet well understood. As a consequence,

a considerable number of patients require more than one procedure to cure their symptoms. Developing techniques for visualizing the ablation scars paves the way for research to better understand the reasons for different outcomes of the procedure.

The ablation scars appear as enhanced areas in delayed enhancement magnetic resonance images (DE-MRI) acquired after the procedure. Unfortunately, there are numerous other areas in the images that are enhanced as well. The key idea in our approach is to take advantage of the fact that the scar is only located on the surface of the left atrium. We first automatically segmented the left atrium in MRA images using the previously described approach and then transferred it to the DE-MRI image of the same patient by registering the two images. We used an affine registration algorithm to correct for small differences in the shape and location of the heart in the two scans. The registration yielded a left atrium segmentation in the DE-MRI image. However, the original left atrium segmentation and the registration between the two images of different modalities are not perfect, and thus the final segmentation might contain errors. We therefore assumed that the scar can be located within a certain small distance of the left atrium segmentation outline. We determined the optimal value for this distance experimentally.

We visualize the ablation scars by performing a maximum intensity projection of the DE-MRI image onto the automatically generated surface of the left atrium. The visualization is further improved by thresholding the projection. We showed visually that both visualizations correlate well with the expert manual segmentation of the ablation scars.

### **Future directions**

While we successfully produced meaningful visualizations of post-procedure ablation scars, our surface projections were two dimensional and thus did not allow for the computation of certain relevant measures, such as the scar volume. An interesting topic of future research would be to perform segmentation of the scars in the 3-dimensional DE-MRI images. However, even with prior knowledge in the form of the left atrium segmentation, this is still a difficult task because of the low contrast ratio

and high noise in the images.

An entirely different direction would be to examine the topology of the scars from either our surface scar projections or 3-dimensional segmentations, with the goal of correlating measures of the scar shape and volume with the procedure outcomes. There are numerous possible approaches to this problem. One of them would be to characterize the variations in shape and topology of the scars by finding sub-groups in the population based on these variations. This idea could be pushed even further by factoring in the anatomical variations of the left atrium shape. This extension would model the relationship between the procedure outcome and the scar topology differently depending on the shape and anatomical configuration of the left atrium. The proposed developments would enable deeper understanding of cardiac ablation procedures with the end goal of helping surgeons improve their success rate and by doing so improving the patients' lives.



# Bibliography

- [1] Vincent Arsigny, Olivier Commowick, Xavier Pennec, and Nicholas Ayache. A log-euclidean framework for statistics on diffeomorphisms. In *Medical Image Computing and Computer-Assisted Intervention*, pages 924–931, 2006.
- [2] Matias Bossa, Monica Hernandez, and Salvador Olmos. Contributions to 3d diffeomorphic atlas estimation: Application to brain images. In *Medical Image Computing and Computer-Assisted Intervention*, pages 667–674, 2007.
- [3] Morten Bro-Nielsen and Claus Gramkow. Fast fluid registration of medical images. In *International Conference on Visualization in Biomedical Computing*, pages 267–276, 1996.
- [4] Yong-Mei Cha, Margaret M. Redfield, Win-Kuang Shen, and Bernard J. Gersh. Atrial fibrillation and ventricular dysfunction: a vicious electromechanical cycle. *Circulation*, 109:2839–2843, 2004.
- [5] Gary E. Christensen, Richard D. Rabbitt, and Michael I. Miller. Deformable templates using large deformation kinematics. *IEEE Transactions on Image Processing*, 5(10):1435–1446, October 1996.
- [6] Several Contributors. 3D Slicer: A multi-platform, free and open source software package for visualization and medical image computing. <http://www.slicer.org/>, August 2010.
- [7] Michal Depa, Mert R. Sabuncu, Ehud J. Schmidt Godtfred Holmvang, Reza Nezafat, and Polina Golland. Robust atlas-based segmentation of highly variable anatomy: Left atrium segmentation. In *MICCAI Workshop on Statistical Atlases and Computational Models of the Heart: Mapping Structure and Function*, pages 85–94, September 2010.
- [8] Lee R. Dice. Measures of the amount of ecologic association between species. *Ecology*, 26(3):297–302, 1945.
- [9] Florence Dru and Tom Vercauteren. An itk implementation of the symmetric log-domain diffeomorphic demons algorithm. *Insight Journal*, May 2009.
- [10] Srinivas R. Dukkupati, Richard Mallozzi, Ehud J. Schmidt, Godtfred Holmvang, Andre d’Avila, Renee Guhde, Robert D. Darrow, Glenn Slavin, Maggie

- Fung, Zachary Malchano, Greg Kampa, Jeremy D. Dando, Christina McPherson, Thomas K. Foo, Jeremy N. Ruskin, Charles L. Dumoulin, and Vivek Y. Reddy. Electroanatomic mapping of the left ventricle in a porcine model of chronic myocardial infarction with magnetic resonance-based catheter tracking. *Circulation*, August 2008.
- [11] Olivier Ecabert, Jochen Peters, and Jürgen Weese. Modeling shape variability for full heart segmentation in cardiac computed-tomography images. In *SPIE Medical Imaging 2006: Image Processing*, 2006.
- [12] Kenneth M. Flegel, Martin J. Shipley, and Geoffrey Rose. Risk of stroke in non-rheumatic atrial fibrillation. *Lancet*, 1:526–529, 1987.
- [13] Alexandre Guimond, Alexis Roche, Nicholas Ayache, and Jean Meunier. Three-dimensional multimodal brain warping using the demons algorithm and adaptive intensity corrections. *IEEE Transactions on Medical Imaging*, 20(1):58–69, January 2001.
- [14] Henry R. Halperin and Sama Nazarian. Damage assessment after ablation. *Journal of the American College of Cardiology*, pages 1272–1273, 2008.
- [15] Rolf A. Heckemann, Joseph V. Hajnal, Paul Aljabar, Daniel Rueckert, and Alexander Hammers. Automatic anatomical brain MRI segmentation combining label propagation and decision fusion. *Neuroimage*, 33(1):115–126, 2006.
- [16] Li-Yueh Hsu, W. Patricia Ingkanisorn, Peter Kellman, Anthony H. Aletras, and Andrew E. Arai. Quantitative myocardial infarction on delayed enhancement MRI. Part II: Clinical application of an automated feature analysis and combined thresholding infarct sizing algorithm. *Journal of magnetic resonance imaging : JMRI*, 23(3):309–14, March 2006.
- [17] Li-Yueh Hsu, Alex Natanzon, Peter Kellman, Glenn A. Hirsch, Anthony H. Aletras, and Andrew E. Arai. Quantitative myocardial infarction on delayed enhancement MRI. Part I: Animal validation of an automated feature analysis and combined thresholding infarct sizing algorithm. *Journal of magnetic resonance imaging : JMRI*, 23(3):298–308, March 2006.
- [18] Luis Ibáñez, Will Schroeder, Lydia Ng, and Josh Cates. *The ITK Software Guide*. Kitware, Inc., 2.4 edition, 2005.
- [19] Yuri Ishihara, Reza Nazafat, John V. Wylie, Marius G. Linguraru, Mark E. Josephson, Robert D. Howe, Warren J. Manning, and Dana C. Peters. MRI evaluation of RF ablation scarring for atrial fibrillation treatment. In *SPIE Medical Imaging 2007: Visualization and Image-Guided Procedures*, 2007.
- [20] Matthias John and Norbert Rahn. Automatic left atrium segmentation by cutting the blood pool at narrowings. In *Medical Image Computing and Computer-Assisted Intervention*, pages 798–805, September 2005.

- [21] Rashed Karim, Raad Mohiaddin, and Daniel Rueckert. Left atrium segmentation for atrial fibrillation ablation. In *SPIE Medical Imaging 2008: Visualization, Image-guided Procedures, and Modeling*, 2008.
- [22] Koen Van Leemput, F. Maes, D Vandermeulen, and P. Seutens. Automated model-based tissue classification of MR images of the brain. *IEEE Transactions on Medical Imaging*, 18(10):897–908, October 1999.
- [23] William E. Lorensen and Harvey E. Cline. Marching cubes: A high resolution 3D surface construction algorithm. In *Proceedings of the 14th Annual Conference on Computer Graphics and Interactive Techniques*, SIGGRAPH 1987, pages 163–169, New York, NY, USA, 1987. ACM.
- [24] Cristian Lorenz and Jens von Berg. A comprehensive shape model of the heart. *Medical Image Analysis*, 10(4):657–670, 2006.
- [25] Christopher J. McGann, Eugene G. Kholmovski, Robert S. Oakes, Joshua J.E. Blauer, Marcos Daccarett, Nathan Segerson, Kelly J. Airey, Nazem Akoum, Eric Fish, Troy J. Badger, Edward V.R. DiBella, Dennis Parker, Rob S. MacLeod, and Nassir F. Marrouche. New magnetic resonance imaging-based method for defining the extent of left atrial wall injury after the ablation of atrial fibrillation. *Journal of the American College of Cardiology*, pages 1263–1271, May 2008.
- [26] Vivek Y. Reddy, Ehud J. Schmidt, Godtfred Holmvang, and Maggie Fung. Arrhythmia recurrence after atrial fibrillation ablation: Can magnetic resonance imaging identify gaps in atrial ablation lines? *Journal of Cardiovascular Electrophysiology*, pages 434–437, 2007.
- [27] Daniel Rueckert, L. I. Sonoda, C. Hayes, D. L. G. Hill, M. O. Leach, and D. J. Hawkes. Nonrigid registration using free-form deformations: Application to breast mr images. *IEEE Transactions on Medical Imaging*, 18(8):429–442, August 1999.
- [28] Mert R. Sabuncu, S. K. Balci, M. E. Shenton, and P. Golland. Image-driven population analysis through mixture modeling. *IEEE Transactions on Medical Imaging*, 28(9):1473–1487, 2009.
- [29] Mert R. Sabuncu, B.T.T. Yeo, K. Van Leemput, B. Fischl, and P. Golland. A generative model for image segmentation based on label fusion. *Medical Imaging, IEEE Transactions on*, 29(10):1714–1729, October 2010.
- [30] Ehud J. Schmidt, Richard P. Mallozzi, Aravinda Thiagalingam, Godtfred Holmvang, Andre d’Avila, Renee Guhde, Robert Darrow, Glenn Slavin, Maggie Fung, Jeremy Dando, Lori Foley, Charles Dumoulin, and Vivek Reddy. Electroanatomic mapping and radiofrequency ablation of porcine left atria and atrioventricular nodes using magnetic resonance catheter tracking. *Circulation*, 2009.

- [31] Jason E. Taclas, Reza Nezafat, John V. Wylie, Mark E. Josephson, Jeff Hsing, Warren J. Manning, and Dana C. Peters. Relationship between intended sites of RF ablation and post-procedural scar in af patients, using late gadolinium enhancement cardiovascular magnetic resonance. *Heart rhythm : the official journal of the Heart Rhythm Society*, 7(4):489–496, 2010.
- [32] Jean-Philippe Thirion. Image matching as a diffusion process: an analogy with maxwell’s demons. *Medical Image Analysis*, 2(3):243–260, 1998.
- [33] Tom Vercauteren, Xavier Pennec, Aymeric Perchant, and Nicholas Ayache. Symmetric log-domain diffeomorphic registration: A demons-based approach. In *Medical Image Computing and Computer-Assisted Intervention*, pages 754–761, 2008.
- [34] William M. Wells, W. Eric L. Grimson, Ron Kikinis, and Ferenc A. Jolesz. Adaptive segmentation of MRI data. *IEEE Transactions on Medical Imaging*, 15(4):429–442, August 1996.
- [35] William M. Wells, Paul Viola, Hideki Atsumi, Shin Nakajima, and Ron Kikinis. Multi-modal volume registration by maximization of mutual information. *Medical Image Analysis*, 1(1):35–51, 1996.
- [36] Yefeng Zheng, Adrian Barbu, Bogdan Georgescu, Michael Scheuering, and Dorin Comaniciu. Four-chamber heart modeling and automatic segmentation for 3D cardiac CT volumes using marginal space learning and steerable features. *IEEE Transactions on Medical Imaging*, 27(11):1668–1681, November 2008.